JGR Earth Surface

RESEARCH ARTICLE
10.1029/2022JF006948

Special Section:
Forcing, response, and impacts of coastal storms in a changing climate

Geomorphic Response of a Coastal Berm to Storm Surge and the Importance of Sheet Flow Dynamics

M. Pontiki[1], J. A. Puleo[1], H. Bond[2], M. Wengrove[2], R. A. Feagin[3,4], T.-J. Hsu[1], and T. Huff[3]

[1]Department of Civil and Environmental Engineering, University of Delaware, Newark, DE, USA, [2]Department of Civil and Construction Engineering, Oregon State University, Corvallis, OR, USA, [3]Department of Ecology and Conservation Biology, Texas A&M University, College Station, TX, USA, [4]Department of Ocean Engineering, Texas A&M University, College Station, TX, USA

Abstract During a storm, as the beach profile is impacted by increased wave forcing and rapidly changing water levels, sand berms may help mitigate erosion of the backshore. However, the mechanics of berm morphodynamics have not been fully described. In this study, 26 trials were conducted in a large wave flume to explore the response of a near-prototype berm to scaled storm conditions. Sensors were used to quantify hydrodynamics, sheet flow dynamics, and berm evolution. Results indicate that berm overtopping and offshore sediment transport were key processes causing berm erosion. During the morphological evolution of the beach profile, two sand bars were formed offshore that attenuated subsequent wave energy. The landward extent of that energy was confined to the seaward foreshore, inhibiting inundation of the backshore. Net offshore-directed transport was dominant when infragravity motions increased in the swash zone. Conversely, the influence of incident-band motions on sediment transport was relatively greater in the inner-surf zone. Near-bed flow velocities and sheet flow layer thicknesses were larger in the swash zone than in the inner-surf zone. This paper also provides a valuable analysis between morphology-estimated total sediment transport rates and rates derived from in situ measurements. Sheet flow dynamics dominated foreshore cross-shore sediment processes, constituting the largest portion of the total sediment transport load throughout the berm erosion.

Plain Language Summary Coastal berms are natural sand barriers between the ocean and the back beach. During storms, berms may help prevent or slow down the erosion of the beach. A large-scale laboratory experiment was conducted to study sediment transport and how berms erode. Sensors were used to measure water levels, flow velocities, sediment concentrations, and beach profile changes. The findings indicate that berm erosion was primarily caused by swash processes occurring as waves overtopped the berm. Offshore sediment transport resulted in the formation of two sand bars that helped dissipate subsequent wave energy. Overall, by quantifying processes leading to berm erosion, we can enhance our understanding of coastal dynamics, implement effective measures to protect beaches during storms, and safeguard against flooding.

Key Points:

- Wave overtopping, runup, and low-frequency motions are the main processes of berm erosion
- During early storm stages, near-bed flow velocities and sheet layer thicknesses are larger in the swash zone than in the inner-surf zone
- Quantification of sediment transport rates indicates the dominance of sheet flow layer load at the foreshore, throughout the berm erosion

Correspondence to:
M. Pontiki,
mpontiki@udel.edu

Citation:
Pontiki, M., Puleo, J. A., Bond, H., Wengrove, M., Feagin, R. A., Hsu, T.-J., & Huff, T. (2023). Geomorphic response of a coastal berm to storm surge and the importance of sheet flow dynamics. *Journal of Geophysical Research: Earth Surface*, *128*, e2022JF006948. https://doi.org/10.1029/2022JF006948

Received 1 OCT 2022
Accepted 22 SEP 2023
Corrected 3 NOV 2023

This article was corrected on 3 NOV 2023. See the end of the full text for details.

Author Contributions:
Conceptualization: J. A. Puleo, R. A. Feagin
Data curation: M. Pontiki, H. Bond, T. Huff
Formal analysis: M. Pontiki
Funding acquisition: J. A. Puleo, M. Wengrove, R. A. Feagin, T.-J. Hsu
Investigation: M. Pontiki
Methodology: M. Pontiki, J. A. Puleo

1. Introduction

Berms are pronounced shore-parallel morphological features located near the mean water level of many beaches. Berm slopes are usually steep on the seaward edge and milder on the landward flank (Figure 1). In a low-energy system, berms form naturally while the beach steepens under swash action and migrate onshore during high tides through overwash processes (Figlus et al., 2012; Hine, 1979). They may also be artificially constructed as a part of a beach replenishment project with sand deposited in the nearshore or swash zone (Brutsché et al., 2015; Zhu et al., 2022). During storms, large waves and water levels exceeding astronomical high tides trigger offshore sediment transport, reducing the berm prominence. Thus, berms constitute a line of the coastal flood defense system that dissipates wave energy via sacrificial erosion.

Berm evolution has been studied using a variety of methodologies. Conceptual models have been created by analyzing the historical trends of beach erosion (Katoh & Yanagishima, 2015; Mizuguchi & Seki, 2015; Suzuki et al., 2007) and pre- and post-storm field survey data (Beuzen et al., 2019; Jensen et al., 2009; Phillips et al., 2019). Intra-storm wave energy fluxes and runup (Suzuki et al., 2007), and infragravity motion along with elevated water levels (Katoh & Yanagishima, 2015; Mizuguchi & Seki, 2015), have been determined to play a key role in berm erosion. Suzuki et al. (2007) approximated sediment transport rates on an eroding berm with inverse sediment transport estimates after examining spatio-temporal beach profile transformations. However,

Project Administration: J. A. Puleo, M. Wengrove, R. A. Feagin, T.-J. Hsu
Supervision: J. A. Puleo, M. Wengrove, R. A. Feagin
Validation: M. Pontiki
Visualization: M. Pontiki
Writing – original draft: M. Pontiki
Writing – review & editing: M. Pontiki, J. A. Puleo, H. Bond, M. Wengrove, R. A. Feagin, T.-J. Hsu, T. Huff

the results were not substantiated by direct sediment load measurements. Small-scale experiments have yielded further insights into the berm geometry impact on cross-shore sediment transport rates and beach profile temporal variations (Figlus et al., 2012; Kobayashi et al., 2009). However, these laboratory studies were limited by scale effects and the absence of sensors capable of measuring sediment concentrations near the bed.

Brutsché et al. (2015) found that the longevity of nearshore sand placements may be enhanced by expanding the extent of berms alongshore, but that their performance is not improved by increased berm elevation. The effect of intense, short-term events on berm nourishment placed in the swash zone has been explored under the auspices of the equilibrium beach profile concept (Brutsché et al., 2015; P. Wang et al., 2013), albeit the parameters included in these models are not well-related to post-storm beach deformations. During the storm forcing, the balance between the destructive and constructive forces acting on the coast may be disrupted and thus the distortive mechanisms differ from those observed during short-term shoreline recession.

Beach erosion patterns arise from cross-shore and alongshore gradients in the sediment transport rate at a site (Dean & Dalrymple, 2002; Komar, 1998). The total sediment load results from the simultaneous contributions of different transport modes: the suspended load and bedload or sheet flow (Nielsen, 2009). Bedload is characterized by transport supported by inter-particle collisions (Bagnold, 1956). Sheet flow consists of a highly concentrated thin layer of mobilized sediment over the undisturbed bed (O'Donoghue & Wright, 2004). The sheet flow layer thickness varies from millimeters (Dohmen-Janssen & Hanes, 2005) to centimeters (Lanckriet et al., 2014) depending on the flow regime and cross-shore location on the beach profile. In the swash zone, sheet flow thickness increases almost instantaneously upon uprush arrival, decreases throughout flow reversal (Lanckriet et al., 2014), and increases again throughout most of backwash until the flow thins and friction processes prevail (Masselink & Puleo, 2006). Sheet flow dynamics are likely to dominate near-bed processes under energetic forcing when excess shear stress is large (Horikawa et al., 1982; Myrhaug & Holmedal, 2007). These processes have been examined under non-breaking wave groups (Dohmen-Janssen & Hanes, 2005), under bichromatic waves (van der Zanden et al., 2015), and in swash zone field studies (Lanckriet et al., 2014; Puleo et al., 2014; Yu et al., 1990).

Despite recent advances in understanding the response of natural berms and berm nourishment to extreme waves and storm surges, data are lacking that relate sheet flow dynamics to berm erosion during a storm event. The objective of this paper is to explore the temporal berm evolution during energetic forcing and associate it with inner-inner- and swash zone dynamics, using measurements collected in a near-prototype experiment.

2. Methodology

Physical model tests were performed in the 104 × 3.7 × 4.6 m NSF NHERI large wave flume (Figure 2) at the O.H. Hinsdale Wave Research Laboratory, Oregon State University, Corvallis, OR, USA, to obtain simultaneous measurements of wave forcing, currents, sediment transport, and morphodynamics. A pre-storm beach profile from Mantoloking, New Jersey, USA, typical of many sandy beaches (Luijendijk et al., 2018) was simulated (Feagin et al., 2023). The beach profile was constructed after applying scaling laws (Equations 1 and 2, Van Rijn et al., 2011) using natural sand sourced from South Beach in Newport, Oregon. The median sediment diameter, d_{50}, of the 105 sand used was 0.21 mm. In comparison, the d_{50} value for Mantoloking Beach is 0.39 mm. The sand was installed in roughly 0.3 m lifts and compacted with a vibratory plate compactor (~25"). The depth and sediment model values were included in the scaling computations as free parameters based on the flume dimensions and the d_{50}. The length scale and distortion scale were imposed when the depth scale and the sediment scale were defined (Equation 1). The time scale followed from Equation 2 as,

$$n_l = n_h\, {n_{d50}}^{-0.5}\, {n_h}^{0.28}\, {n_{s-1}}^{-0.5} \tag{1}$$

$$n_{Tm} = {n_h}^{0.56}, \tag{2}$$

where $n_l = 2.35$ is the length scale, $n_h = 2.5$ is the depth scale, $n_{d50} = 1.89$ is the sediment size scale, n_{s-1} is the relative density scale and n_{Tm} is the morphological time scale. Assuming a sediment density, ρ_s of 2,650 kg/m^3, and freshwater density, ρ_w of 1,000 kg/m^3, the relative density is $s = \rho_s/\rho_w = 2.65$, and $n_{s-1} = 1$.

The waves and water levels used in the study were based on scaled conditions. A scaled segment of waves was derived using the third-generation wave model WAVEWATCH III (WW3DG - The WAVEWATCH III®

Figure 1. Subaerial beach during post-storm wave conditions at Coin Beach, Delaware, U.S.A (38.61°N, 75.06°W) on 12 February 2021, showing an eroded berm. Swash flow (a) running up the breached berm (b). Foam exists between the runnel (c) and the scarped dune front (d).

Development Group, 2016), based on modeled wave conditions that occurred between 29 and 30 October 2012 as driven by Hurricane Sandy off the coast of Mantoloking (40.12° N, 74.00°W). Water levels obtained from the National Oceanic and Atmospheric Administration (NOAA) buoy 8534720 near Atlantic City, New Jersey, during Hurricane Sandy, were also scaled for the study. The examined storm sequence was discretized into short trial intervals to enable intermittent profile surveying and sensor adjustment. A total of 47 trials were conducted varying the water level from 2 to 2.74 m and the spectral significant wave height from 0.20 to 0.97 m. Each trial consisted of 300 waves.

The response of the berm to varying wave heights and water levels was investigated during the first 26 trials (T01–T26) representing 590 min of the storm (Tables 1 and 2). The irregular waves followed a TMA shallow water spectrum (Bouws et al., 1985; ITTC, 2002) and were generated with a piston wave maker equipped with active absorption. The number of waves, N_w, generated per trial denotes the trial interval duration, D, which varied according to the peak wave periods. H_{m0} is the spectral significant wave height, T_p is the period associated with the most energetic waves in the wave spectrum, and h is the water depth measured offshore at x = 14 m, from the bottom of the flume to the still water surface.

The investigation of berm changes and sheet flow dynamics required a range of sensors to be deployed. Measurements were obtained; offshore and at four instrument stations installed in the berm region (ST1,

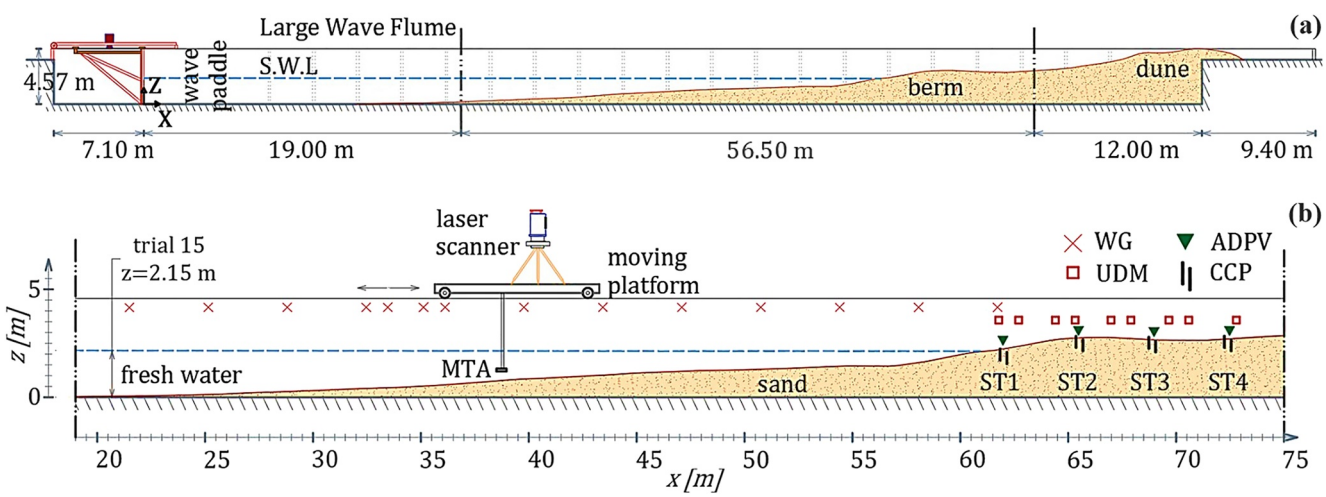

Figure 2. Sectional drawings of the experimental setup. Large Wave Flume and simulated beach profile between x = 19–75.5 m (a). Schematic of the examined area in this study (the region between the two vertical dashed lines in panel (a)), and sensor deployment (b). The locations of wave gauges, ultrasonic distance meters, acoustic Doppler profiling velocimeters, and conductivity concentration profilers at the four sensor stations (ST1–ST4, x = 62.28–73.04 m) are denoted.

Table 1
Wave Conditions and Water Depths at x = 14 m During Trials 1–13

	T01	T02	T03	T04	T05	T06	T07	T08	T09	T10	T11	T12	T13
D (min)	8	17	8	15	23	23	23	24	24	24	24	25	25
N_w (–)	345	422	154	302	453	439	445	475	463	457	447	459	450
H_{m0} (m)	0.20	0.40	0.62	0.62	0.63	0.64	0.65	0.66	0.67	0.69	0.70	0.71	0.72
T_p (s)	1.53	3.35	4.49	4.50	4.54	4.60	4.65	4.71	4.76	4.82	4.88	4.93	4.99
h (m)	2.02	2.05	2.10	2.10	2.11	2.11	2.12	2.12	2.13	2.13	2.14	2.14	2.15

x = 62.28 m; ST2, x = 65.04 m; ST3, x = 69.59 m; ST4, x = 73.04 m). Fourteen capacitance wave gauges (WGs), seven ultrasonic distance meters (UDMs), four acoustic Doppler profiling velocimeters (ADPVs), and eight conductivity concentration profilers (CCPs) were installed to measure Sheet flow sediment concentrations (SFSC), wave properties, and near-bed velocity profiles (Appendix B3). Additionally, a terrestrial laser scanner quantified berm morphodynamics. Bathymetry variations were monitored with multiple transducer arrays (MTA). Further details regarding the instrumentation and analysis of the data collected are presented in Appendices A and B.

3. Results

3.1. Berm Evolution

A data set of 26 laser scans, collected on the flume centerline transect at the end of each trial, was used to assess the influence of early storm stages on berm evolution (Figure 3; Appendix B1). Bed level progression was considered for x = 23–76 m identifying the most energetic zones: the berm region, x = 59–73 m, the inner sandbar, x = 47–53 m, and the outer sandbar, x = 38–47 m. Increasing hydrodynamic forces impacted the spatial and temporal response patterns of the berm. Spectral significant wave heights, H_{m0}, ranged from 0.20 to 0.62 m between T01 and T04 and initiated berm scarping and a small slope shift from 1:8 to 1:7 from x = 59 m to x = 64.5 m. During these trials, the berm crest was truncated, and sediment accumulated between x = 49 m and x = 53 m. After T05, inner-surf zone processes prevailed at the seaward berm slope, while swash zone processes translated to the berm crest. Waves overtopped the berm crest, but uprush flows did not reach the berm lee side until T12. The berm eroded fully after T13 with offshore-directed sediment transport causing sand bar development at x = 43 m. The berm became more vulnerable to erosion with uprush flow reaching its lee side following berm erosion. Nevertheless, some sediment accretion was observed at the landward end of the berm lee side from T14 to T26, regardless of the continuous foreshore damage. The beach profile collected after T14 revealed a milder foreshore slope of 1:14. By the end of T26, the total sand volume loss was 63.6 m^3 in the berm region.

Volumetric variations were estimated by computing elevation differences between successive profiles. Volume fractions were evaluated as the volume of the features after each trial over their initial volumes and they are expressed in percentages (Figure 4a). Berm volume decrease and sandbar growth are examined considering the water depths above the berm crest and sandbars, respectively (Figure 4b). The berm eroded gradually with the greatest sand losses observed before T09 and near T22, with the water depth increasing linearly from 0 to 0.7 m at the berm crest. The growth of the inner sand bar decelerated after the berm crest eroded completely and the foreshore retreated during T14. The maximum water depths, h_{max}, recorded in the sandbar region remained

Table 2
Wave Conditions and Water Depths at x = 14 m During Trials 14–26

	T14	T15	T16	T17	T18	T19	T20	T21	T22	T23	T24	T25	T26
D (min)	25	26	26	26	26	27	27	27	28	28	29	10	20
N_w (–)	472	473	476	475	484	472	474	469	475	458	483	162	339
H_{m0} (m)	0.73	0.74	0.75	0.77	0.78	0.79	0.80	0.81	0.82	0.83	0.84	0.85	0.85
T_p (s)	5.05	5.11	5.18	5.24	5.30	5.37	5.43	5.50	5.56	5.63	5.70	5.77	5.77
h (m)	2.15	2.15	2.16	2.17	2.18	2.19	2.20	2.21	2.22	2.23	2.24	2.25	2.25

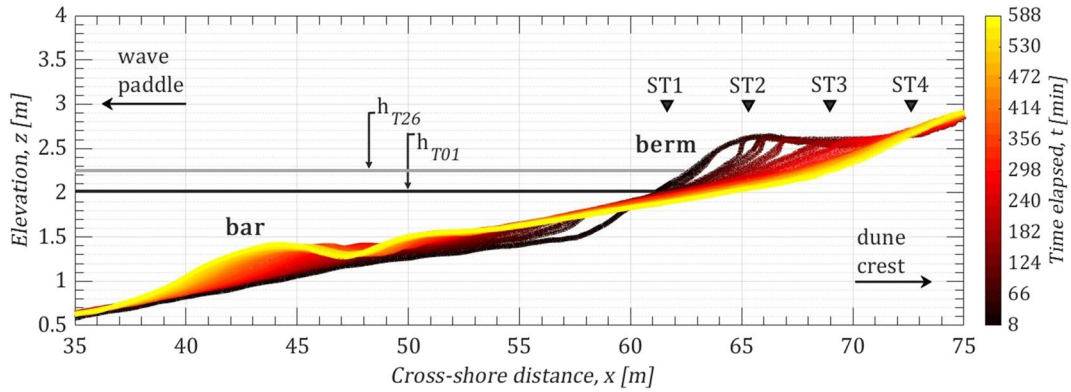

Figure 3. Profile changes in response to amplifying hydrodynamic forces. Instantaneous flow velocities and concentrations were collected between the berm seaward slope and the landward end of the berm lee side. h_{Ti} marks the water depths through berm erosion for trial i at certain locations.

around 1.2 m between T09 and T17 despite the continuously increasing forcing conditions owing to the growth of the sand features and wave breaking around $x = 45$ m.

The rates of sand volume changes and the bed-level progression across the beach profile are also examined (Figure 5). The erosion of the berm triggered offshore sediment transport. As the beach face retreated landwards (≥T11), the outer sandbar volume increased rapidly with a trough generated between the two features at $x = 47$–50 m (Figure 5a—I). Fewer volume losses occurred offshore, $x = 26$–37 m (Figure 5a—II). The largest sand volumes were deposited between $x = 41$–58 m, increasing the bed elevation locally by more than 0.6 m. Less accretion was observed at the lee side of the berm (Figure 5a—III). Although the profile changed drastically at the end of the experiment (T26) with the largest vertical variations around the berm crest, swash zone processes at the preliminary stages of the study resulted in greater volume change rates, with $|\Delta V/\Delta t| > 2$ m^3/m/s (Figure 5a—IV). Notably, the location of the berm toe ($x = 58.5$ m) set the offshore edge of beach erosion as the berm region migrated landward flattening the profile.

The locations of the maximum wave heights, H_{max} (Figure 5a; dotted yellow line), and significant wave heights, H_s (Figure 5b) were evaluated considering the free-surface elevation time series. H_{max} values were identified using the zero down-crossing method, detecting the heights between the wave crests and the preceding troughs to comprise steep fronts noted before the wave breaking (IAHR, 1989). H_s was estimated as the mean of the highest one-third of wave heights at each WG cross-shore position up to $x = 61.5$ m. The outer sandbar set the region of the first wave breaking during each trial. The highest waves were observed either at the offshore sandbar side or at the sandbar crest during the most energetic forcing conditions. Furthermore, the cross-shore location of the 2% runup exceedance levels, $R_{u2\%}$, are denoted in Figure 5a. A detailed description of the evaluated $R_{u2\%}$ values is provided in §3.6.

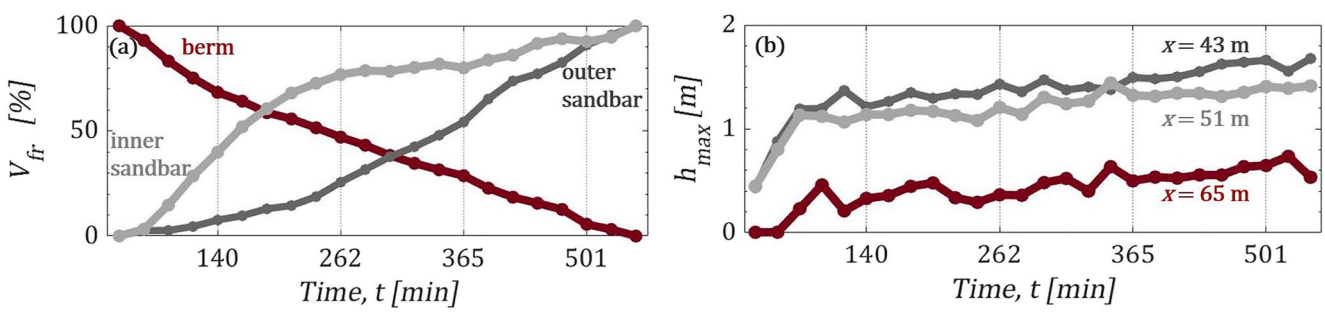

Figure 4. Line plots of the berm and sandbar volume fractions (a). Maximum water depths, h_{max}, recorded over the berm and sandbars during their evolution (b).

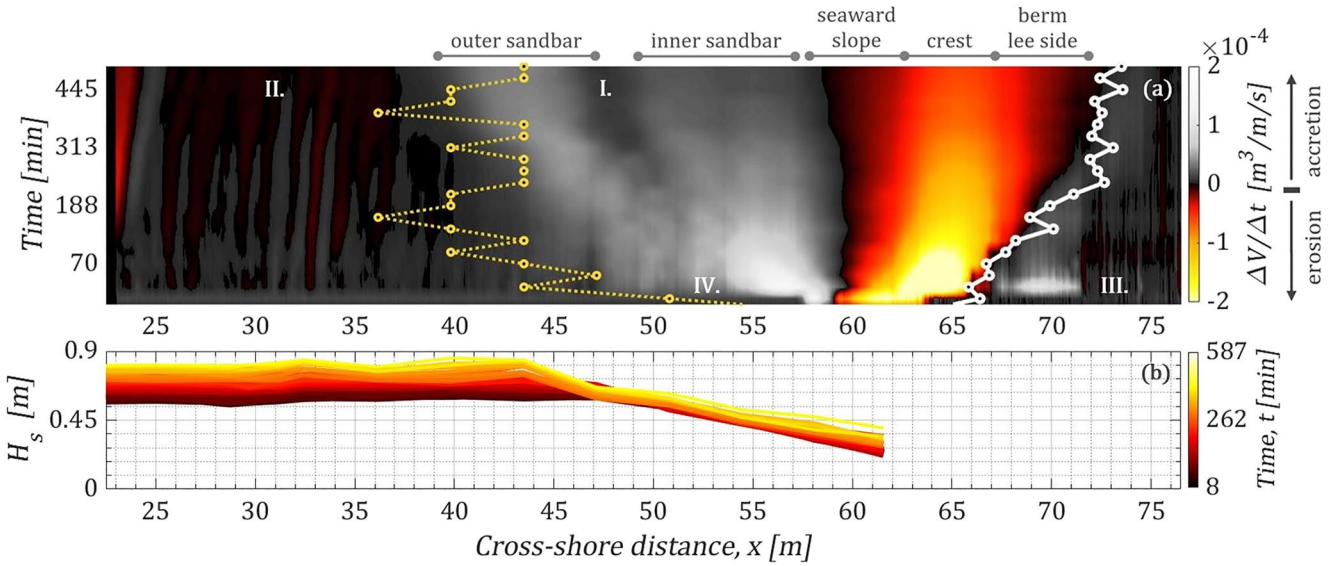

Figure 5. Rates of sand volume changes and the locations of maximum wave heights (dotted yellow line) and 2% runup exceedance (§3.6) levels (solid white line) as a function of time (a). Cross-shore variations of significant wave heights monitored by wave gauges (b).

3.2. Bed Level Fluctuations

The bed-level progression at four locations across the berm is discussed briefly to display the impact of swash processes on berm evolution and the exploitation of the UDM data set (Figure 6; Appendix B). The displayed

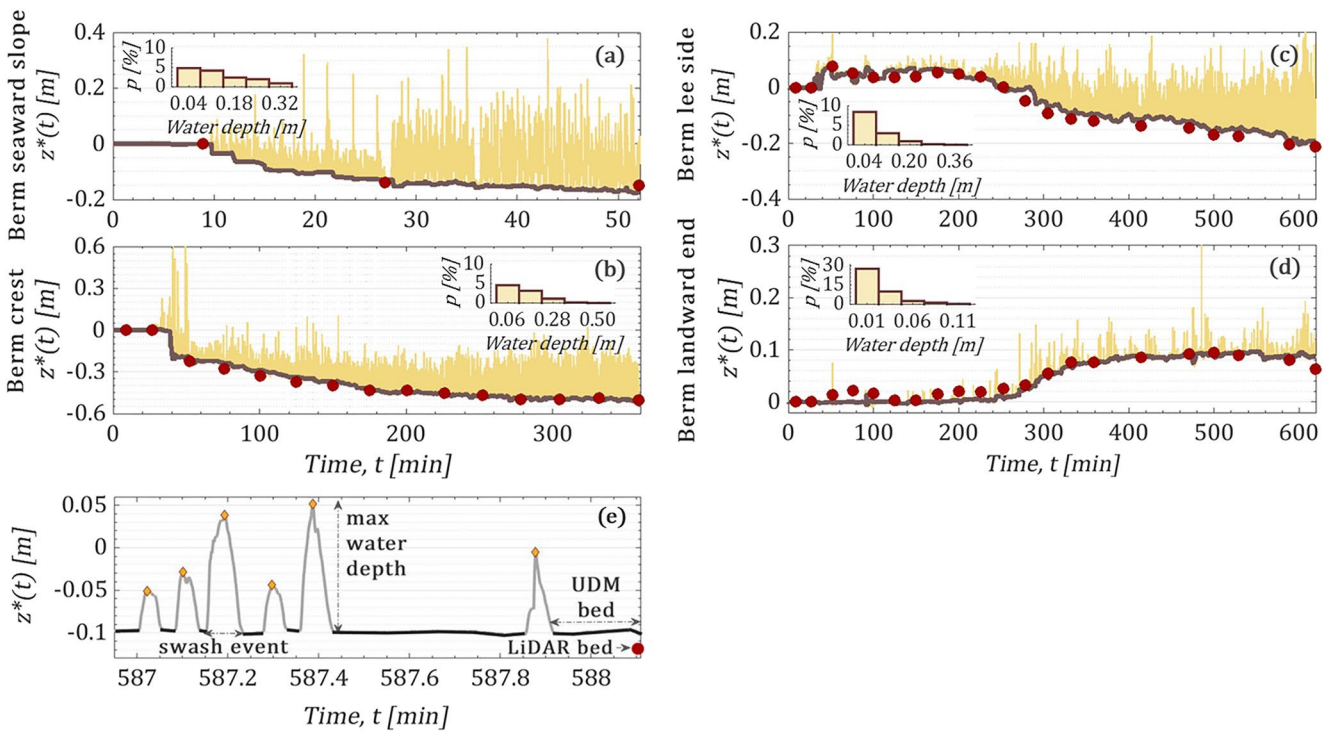

Figure 6. Relative sand surface levels (solid gray line) evaluated from the top of the sheet layer at the beginning of each trial, z^*, and swash events (yellow) measured with the ultrasonic sensors at the berm seaward slope (a) between T01 and T04 at the berm crest (b) between T01 and at berm lee side (c) from T01 to T26 at the landward end of berm lee side (d) from T01 to T26. Ultrasonic distance meter bed-level time series were compared to lidar records (red markers) obtained after each trial. An example of swash peak and swash event identification is displayed (e).

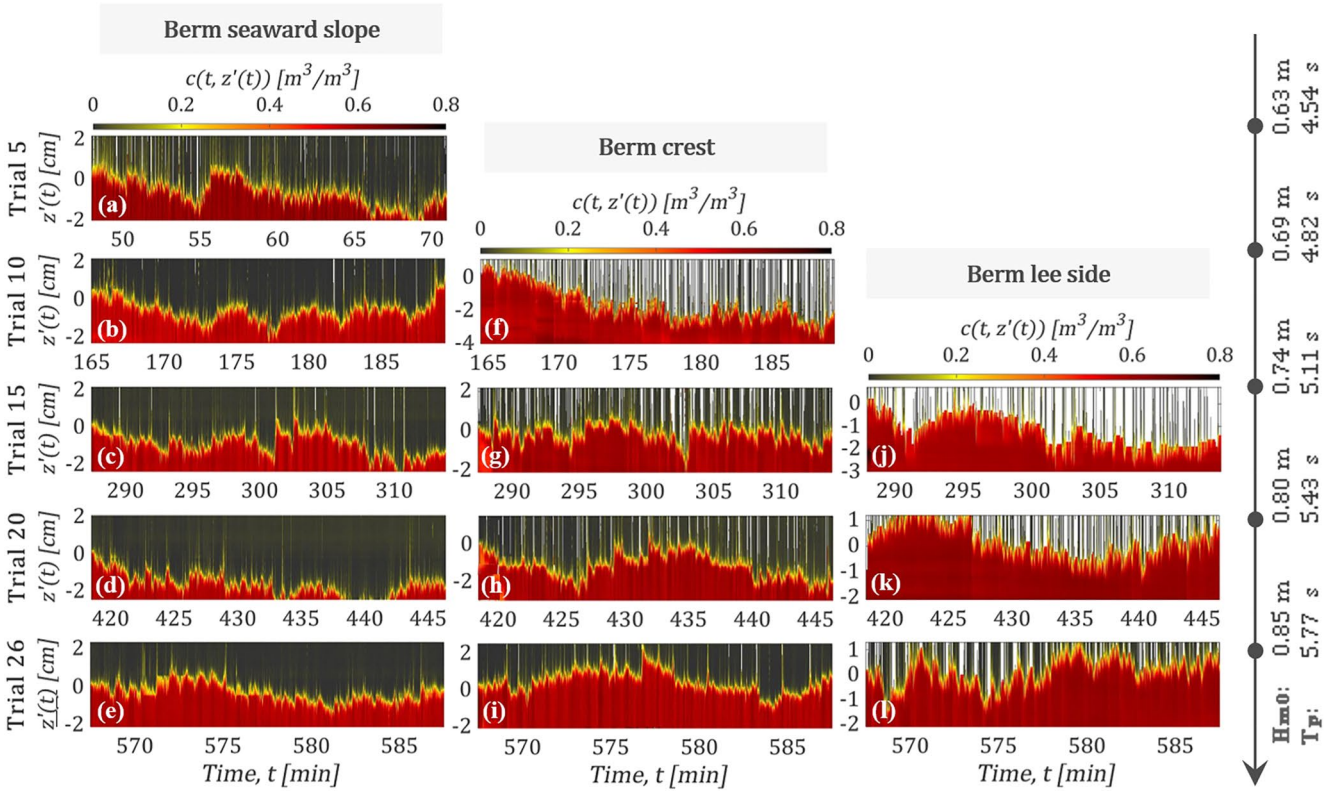

Figure 7. Example conductivity concentration profiler time series. Time-space illustrations of bed-level fluctuations (red), sheet layer time series (yellow), and water presence (gray) over sensor stations (a–e) ST1, (f–i) ST2, and (j–l) ST3. The wave parameters assessed in the respective trials are summarized.

time series spans the duration of swash conditions at the UDM locations and information about the swash depths is summarized in the respective histograms, where p is the probability of swash depth occurrence.

The offshore berm slope was truncated by the incoming waves and swash motions during the early trials T01–T05. By the beginning of T06, the bed at the seaward berm region was fully submerged (Figure 6a) and inner-surf zone processes were monitored. Waves started overtopping the berm crest (Figure 6b) during T05, resulting in bed-level lowering. At the berm lee side, small sediment accretion occurred between T05 and T12 that was followed by bed erosion owing to the rapidly rising water levels and bigger swash events (Figure 6c). Uprush flows and weak bores reached the berm lee side, causing sediment accretion near the dune foot (Figure 6d) between T14 and T26. The histograms suggest that shallower water depths following broken waves in the landward swash zone cause sediment deposition despite the higher energy throughout the trials.

The CCP time series exhibits bed-level variations indicating sediment accretion and erosion patterns in the berm region (Figure 7). The depicted elevations are relative to the level of the sheet layer bottom at the beginning of each trial (Bagnold, 1956; O'Donoghue & Wright, 2004; Appendix B4). Sediment concentrations in the sheet layer were available when the sand surface was submerged or fully saturated (Figures 7d and 7e) and on intra-swash gauges at the seaward (Figures 7a–7c, and 7i), middle (Figures 7g, 7h, and 7l) and landward (Figures 7f, 7j, and 7k) swash zones. During these time intervals, the offshore significant wave height varied from 0.63 to 0.85 m and the offshore water depths increased from 2.02 to 2.25 m. The sand was "dry" at the berm crest, and berm lee side before T10 and T15, respectively.

Incident frequency oscillations are related to the action of breaking waves and small bed-level variations, O(0.001 m), whereas infragravity motions span the time series and are responsible for the general erosional trends. Individual swash events can prompt sudden, large decreases in bed level, O(0.01 m) that are greater than the bed-level variations identified in the inner-surf zone. The subsequent net elevation changes in the landward swash region may vary over 0.02 m, whereas the deviations between the initial and post-trial bed levels in the inner-surf zone are smaller. These differences indicate that swash zone processes trigger sheet

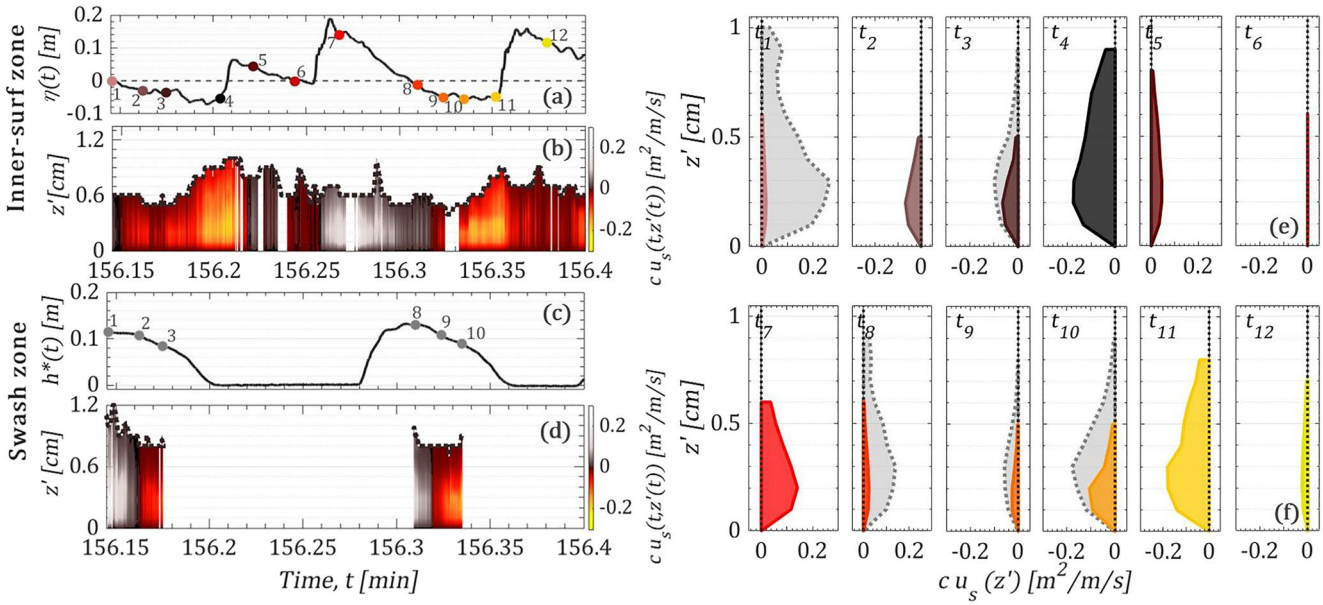

Figure 8. Water surface variations (a) and swash depths (c) associated with instantaneous cross-shore sediment fluxes at the berm seaward slope (b) and berm crest (d), respectively. Inner surf sediment flux profiles (colored shading, solid profile lines) estimated at 12 instances of time (t_1–t_{12}) are compared to the corresponding swash sediment fluxes (gray shading, dotted profile lines) (e, f). Inner surf sediment flux profiles are colored after the associated dots on panels (a, c). Positive values denote onshore-directed sediment flux. Negative fluxes are offshore directed.

flow transport gradients that exceed those in the inner surf zone. The small net bed-level changes in the surf zone (Figure 7e) imply that individual waves may have a minor impact on small time scale bed-level variations. Thus, sheet layer sediment transport gradients are expected to be smaller offshore than those at the landward stations and the swash zone throughout the same time interval (Figures 7i and 7l). Likewise, infragravity motions led to greater bed-level changes at the lee side of the berm (Figures 7j–7l) during and after wave runup and wave overtopping. Despite the more energetic wave conditions offshore and the overall expected bed-level decrease across the subaerial part of the beach profile during later trials, there are sediment depositions of ~0.01 m owing to these low-frequency motions and swash processes at the berm lee side during T20 and T26.

3.3. Sheet Layer Sediment Fluxes

Sediment transport rates, $q(t)$, in the sheet flow layer, were calculated as the depth-integrated product of sheet flow layer concentrations (Appendix B4) and velocities (Appendix B3) as,

$$q(t) = \int_{z'(t)=0}^{\delta_s(t)} c\left(t, z'\right) u_s\left(t, z'\right) dz', \tag{3}$$

where $u_s(t, z')$ is the instantaneous sheet flow velocity profile estimated using Equation B3, Appendix B5, and $c(t, z')$ are the instantaneous SFSC. z' is the elevation from the bottom of sheet flow with respect to the first elevation measurement of the bottom sheet flow layer received at the beginning of each trial at each station.

Flux excerpts and corresponding free surface elevations, η, at the offshore side of the berm and swash depths, h^*, at the berm crest are displayed (Figure 8). Swash depths were evaluated from the top of the sheet layer at the beginning of each trial, z^*, to the free water surface. The maximum spectral significant wave height in the examined trial (T09) was 0.67 m. In the swash zone, T09 water depths were up to 0.43 m with the maximum sheet layer thicknesses not necessarily existing under the deeper swash depths during a swash event. This observation is illustrated between the fluxes computed at 156.15 min with $h^* = 0.1$ m, $\delta s = 0.012$ m, and $cu_{s(z' = 3\ mm)} = 0.28$ m^2/m/s, and in 156.31 min with $h^* = 0.14$ m, $\delta s = 0.009$ m and $cu_{s(z' = 3\ mm)} = 0.17$ m^2/m/s (Figure 8c–8f). Sediment transport is landward directed under positive free surface displacements and uprush flow (swash depth from zero to the peak of a swash event), and offshore directed during negative displacements of the free surface and

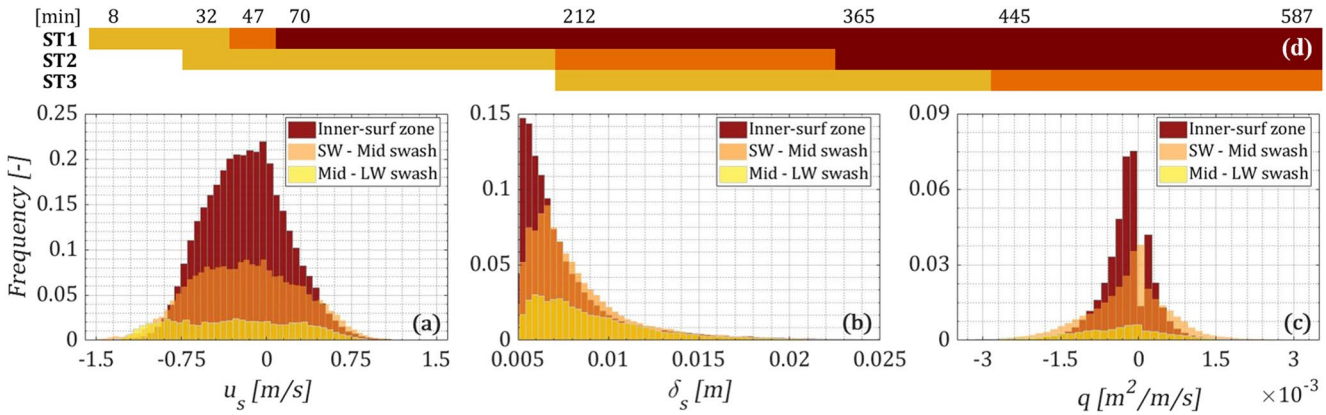

Figure 9. Probability distributions of near-bed flow velocities (a), sheet layer thicknesses (b), and sheet layer fluxes (c) evaluated after considering data at the inner-surf zone (red), seaward (SW) to mid-swash zone (transparent orange), and mid-to landward (LW) swash zone (transparent yellow). The time intervals (in minutes) associated with the data categorization into the three groups are illustrated in the bar chart (d).

backwash motions (swash depths concave downward). Twelve example sheet layer flux profiles are presented (Figures 8e and 8f).

Sediment advection was augmented under the wave crests and troughs in the inner-surf zone. The time series mark phase lag effects in the sheet flow regime that may impact bedload transport (Camenen & Larson, 2006). In the example case, peak flux magnitudes at the berm seaward slope were about 0.18 m^2/m/s. At the berm crest, sediment entrainment occurs only under swash events. Yet, it is evident that more sediment is transported to the landward region of the berm. Besides the thicker mobile bed, the swash fluxes are greater than the inner-surf zone flux magnitudes exceeding 0.2 m^2/m/s at similar sheet flow thicknesses. These observations agree with findings reported in previous studies (Masselink & Puleo, 2006) and further imply the significance of swash zone processes in beach morphodynamics. In general, sediment flux profiles have similar parabolical shapes with inflection points approximately $1/3\delta_s(t)$ above the bottom of the sheet layer. The fluxes decrease toward zero around flow reversal (Figures 8e and 8f; t_6).

3.4. Sheet Flow Processes

Comparison of the sediment transport rates at different cross-shore locations and over time was challenging because of the varying forcing conditions at sensor stations, and the fluctuations of sheet layer sediment fluxes. Sheet layer velocities, sheet flow thicknesses, and sheet layer sediment fluxes are clustered and presented as distributions (Figure 9) considering the processes prevailing at each station. The bar chart summarizes the data classification considering the changes in forcing conditions at the three sensor stations throughout the experiment. Data were tagged in three subsets. The first consisted of inner-surf zone data if the measurement location was constantly submerged at the berm seaward slope from T06 until T26, and at the berm crest from T18 until T26. The second included seaward to mid-swash zone data if the measurement location was submerged 50%–99% of the trial duration (berm seaward slope at T05; berm crest between T11 and T17; berm lee side between T21 and T26). The third subset included mid to landward swash zone data if the measurement location was submerged less than 50% of the trial duration (berm seaward slope between T01 and T04; berm crest between T04 and T10; berm lee side between T12 and T20). Inner surf near-bed flow velocity distributions are roughly bell-curved, whereas the corresponding swash zone flow velocity distributions are more platykurtic and multimodal (Figure 9a). The mid–landward swash distribution appears left-skewed with more frequent greater offshore velocities than the velocities at the lower foreshore and inner-surf zone. The recorded values were primarily between −1.6 m/s and 1.6 m/s with outliers existing up to $|u_s| = 2.8$ m/s.

Figure 9b illustrates the sheet layer thickness distributions that are all right skewed and unimodal and a more gradual tapering toward larger sheet thicknesses. Inner-surf zone sheet layer thicknesses tend to be smaller than those in the swash zone with a mean of 0.007 m and a maximum of 0.023 m. Both the mean and maximum sheet layer thicknesses were larger between the seaward and mid-swash zone with $\delta_{s,\,\mathrm{mean}} = 0.0083$ m and $\delta_{s,\,\mathrm{max}} = 0.034$ m. The inner-surf and seaward swash sediment flux distributions are bell-shaped with narrow peaks,

whereas the mid–landward swash flux distributions are more broadly distributed. This implies that full sediment flux time series are more difficult to obtain where the sand surface is randomly and intermittently covered by water. The outcomes are mainly concentrated within the range of $q \in [-1.5, 1.5]$ m^2/m/s, with fluxes occurring up to $|q| = 4.3$ m^2/m/s. The swash zone sediment flux distributions are heavy-tailed, implying that the frequencies of larger sediment fluxes in this region are greater than those evaluated in the inner-surf zone (Figure 9c).

3.5. Continuity Inversion Estimates of Sediment Transport

Time-sequenced beach profile elevation data can be inverted via the continuity equation to estimate total load sediment transport rates:

$$\frac{\partial q_t}{\partial x} = -(1 - p_r)\frac{\partial z}{\partial t} \quad \rightarrow \quad q_t(x_i) = q_t(x_{i-1}) - (1 - p_r)\int_{x_{i-1}}^{x_i} \frac{\Delta z}{\Delta t}\, dx, \tag{4}$$

where q_t is the total load sediment transport rate at cross-shore location x_i, p_r is the porosity of sand assumed constant across the profile and equal to 0.4, Δz is bed-level differences between consecutive trials at x_i for the duration of Δt, Δt is the time interval of a trial, and dx is the cross-shore spatial distance (0.005 m). Calculations are performed along the flume centerline assuming a uniform profile alongshore and $\partial q/\partial x >> \partial q/\partial y$ (Jensen et al., 2009; van der Zanden et al., 2015). Equation 4 is discretized, and typically applied moving from offshore to onshore or onshore to offshore. Any bias or error in profile elevation data will accumulate along the profile. An option to reduce the bias was to conduct the calculation in both directions and take the average transport rate at each cross-shore location (van der Zanden et al., 2015). This extra calculation does not fully remove the bias, but instead distributes it to both ends of the profile.

Bias or errors in the flume centerline profile data could arise from inherent measurement errors, footfalls of researchers while positioning sensors, the unavailability of porosity data, and lack of 3D morphodynamics data. Other systemic errors are attributed to sensor capabilities. The MTA was unable to measure profile elevation when the water depth was shallower than 0.3 m. The lidar was also unable to measure the profile at these shallow depths owing to the inability of the laser to penetrate the water. Thus, the profiles from the two sensors were merged in this region via interpolation.

Lacking direct knowledge of the error magnitude, an error analysis was performed to assess the magnitude of errors associated with these sources. The estimates for the error magnitudes due to the lidar (E1) and the MTA (E2) accuracies were obtained from the manufacturer specifications (Appendix A). The error magnitude related to the interpolation between the lidar and MTA records (E3) was 0.024 m. This value was computed by weighting the accuracies of the sensors and assuming that the error in the interpolated elevations was solely due to the linearization process. The elevation errors associated with researcher footsteps were assessed around 0.035 m, considering a study discussing the maximum elevation changes owing to footsteps on wet sand (Bates et al., 2013). Furthermore, based on the analysis of Shin (2022), the error magnitude associated with the assumption of constant porosity (E4) could be on the order of 0.015 m and is influenced by factors such as the pore structure. Disregarding 3D morphodynamics could result in inaccuracies in bed topography measurements. The extent of these errors was assumed to be 0.005 m without any records available for robust quantification (E5).

A different approach was taken to implement Equation 4 and minimize the transport estimate bias. A Monte Carlo simulation was developed to account for cumulative error effects (Pontiki, 2022). Uncertainties for each cross-shore location along the profile were assumed random and uncorrelated. Using an uncertainty propagation equation (Equation 5) and the assumed error magnitudes (E1–E5), the local elevation deviations, Y, were estimated to be within ± 0.05 m. Subsequently, a normal distribution was generated considering the Central Limit Theorem and the substantial number of collected data points. Considering the initial beach profile and the profiles recorded after each trial, the model assessed whether there was no balance between the accretion and erosion areas. Depending on when the erosion or deposition area across the profile was larger, the model added or subtracted the local errors from the elevation records. The simulation distributed the uncertainties randomly across the beach profile to minimize the error accumulation at every space step. The errors were iteratively recalculated through the multiple probability simulation until the beach profiles reached a stable state. Local elevation errors decreased drastically by the 2000th iteration from 0.001 to 10^{-10} m and remained stable thereafter. Sediment fluxes were estimated using the revised beach profiles after each iteration.

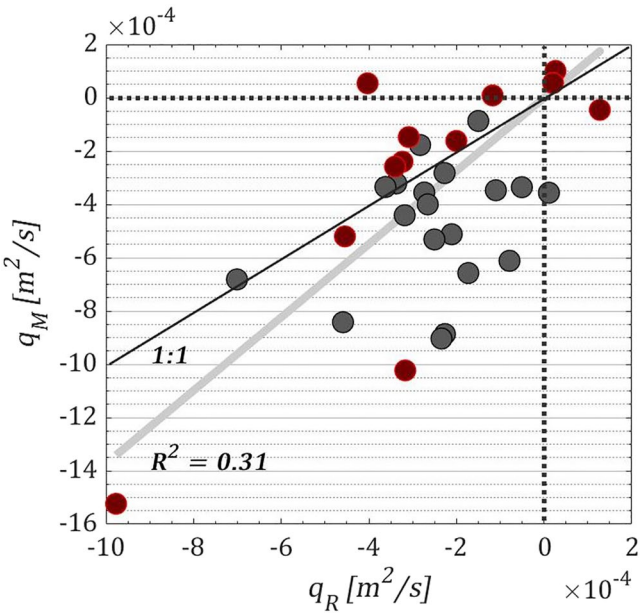

Figure 10. Regression analysis between the total sediment transport rates estimated with the inverse sediment transport equation, q_M, and cumulative sheet layer sediment transport rates approximated using near-bed velocity and sheet layer sediment concentration records, q_R, at the berm seaward slope, berm crest, and berm lee side. The regression line (gray) and the 1:1 line (black) are displayed. Red dots denote results obtained during swash zone processes, whereas gray dots indicate inner-surf zone processes.

$$Y = \sqrt{E_1^2 + E_2^2 + \ldots + E_5^2}, \quad (5)$$

The greatest offshore and onshore sediment transport rates that are up to −2.2 and 1.1 m^2/s at the seaward slope and lee side of the berm, respectively, occurred during the first trials, T02–T10. During this time interval, the largest elevation changes occurred at the seaward swash zone, where the berm slope was truncated and waves overtopped, reaching the backshore, and depositing sediments at the lee side of the berm. Eroded berm sediment accumulated mostly between x = 43 m and x = 47 m where the outer sand bar was created. The offshore transport throughout the trials is designated by persistent negative fluxes in this region. After T23, larger waves were able to reach the landward swash zone and trigger larger offshore-directed sediment transport. Changes among the magnitudes of sediment transport rates were less distinct between T13 and T21. These minor changes in the rates of sediment transport are consistent with the observation of the smaller beach profile variations after the erosion of the berm (§3.1); the formation of the two sand bars led to wave energy dissipation farther from the beach front, inhibiting swash overtopping and thus significant modifications of the beach profile.

Total sediment transport rates per trial at the berm seaward slope, berm crest, and berm lee side were obtained from the morphology data (q_M). The cumulative sediment transport rates estimated from in situ data were named q_R for comparison. Linear regression between q_R and q_M showed that the values are within the same order of magnitude, but with a small coefficient of determination, $R^2 = 0.31$ (Figure 10). The estimated sediment transport directions are consistent for 91% of the q_R and q_M data and conform to the local bed-level progression. Positive values are justified by the accretion patterns at the lee side of the berm (§3.1) during swash events in the earlier trials (T06–T13). In addition, swash zone transport, q_R (red symbols), is either nearly equal to the total transport rates or greater than the suspended sediment transport rates underpinning former findings on the importance of sheet flow layer transport in the swash zone (Komar, 1998). A few swash-zone data points (red symbols) exceed the total, morphology estimated, transport rates by about 0.0001 m^2/s owing to the inability of the sensors to fully capture motions during shallow swash flows. On the contrary, inner surf sheet flow transport rates, q_R (gray symbols), comprise a smaller portion of the total load sediment transport rates as expected.

3.6. Wave Runup and Overtopping

Lidar measurements were used to quantify wave runup and calculate berm overtopping (Figure 11). Sand surface elevation and water-level records were collected along the central transect of the wave flume, allowing the identification of swash events and the detection of bed-level progression. The scans were validated against the ultrasonic sensor readings, giving differences no greater than 0.006 m (§3.2). A swash flow depth cutoff of 0.02 m was used to identify the leading edge of the swash. Spatio-temporal changes in lidar-monitored swash depths were translated to wave runup heights considering the vertical distance between the uprush leading edges and the still water level at the beginning of each trial and the alternating topography. Runup values were discrete values associated with the local maxima identified in the free surface elevation time series.

Two percent runup exceedance heights, $R_{u2\%}$, were used as an indicator of event intensity and parameterization of storm-induced runup (Stockdon et al., 2006; Suanez et al., 2015). $R_{u2\%}$ values were detected in the cumulative probability density functions of discrete runup events as the values exceeded by the largest 2%. Following Holman (1986) $R_{u2\%}$ was related to wave steepness and berm slope, β (Equation 6), using the surf similarity parameter, ξ (Iribarren & Nogales, 1949). Since this approach is relevant for intermediate to reflective foreshores ($0.07 < \tan\beta < 0.2$), extreme runup values were additionally parameterized by $(H_{m0}L_o)^{0.5}$. As the conditions became more dissipative, the beach slope was likely to have a smaller impact on runup processes and thus

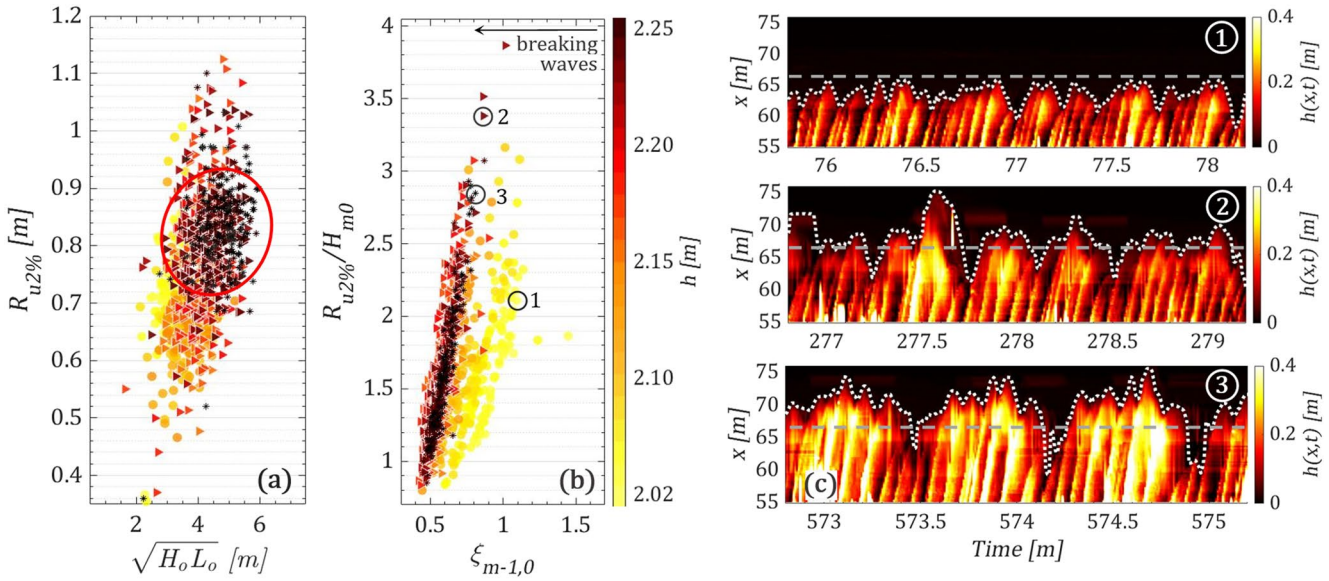

Figure 11. Scatter plot of 2% runup exceedance levels, $R_{u2\%}$, versus offshore wave characteristics, $\sqrt{H_o L_o}$ (a), relative 2% runup height $R_{u2\%}/H_{m0}$ versus the surf similarity parameter $\xi_{m\text{-}1,0}$ (b), flow depths related to uprush motions at the berm region during T05 (c1), T14 (c2), and T26 (c3). Berm crest cross-shore location is indicated with a horizontal dashed line (c). The color bars, h [m], display the varying water depths at the locations of data collection.

berm erosion (Nielsen & Hanslow, 1991). The surf similarity parameter was estimated using offshore wave conditions as,

$$\xi_{m-1,0} = \frac{\tan\beta}{s_{m-1,0}} = \frac{\tan\beta}{\left(\frac{H_{m0}}{L_o}\right)^{0.5}}, \tag{6}$$

where $s_{m-1,0}$ is the wave steepness related to offshore wave spectral parameters, tan β is the mean slope of the berm foreshore, H_{m0} is the offshore spectral significant wave height, L_o is the offshore wavelength (=0.5g$T^2_{m-1,0}/\pi$), and $T_{m-1,0}$ is the spectral wave period. After the complete berm erosion, the mean beach slope between x = 59–73 m is considered for tan β.

Runup data were clustered into distinct records obtained during the three berm erosion stages (Figure 11): the truncation of the berm foreshore (circles), the lowering of the berm crest (triangles), and the complete berm erosion (stars). Scatter plots between the offshore wave characteristics and $R_{u2\%}$ reveal a weak to moderate linear relationship (R^2 ranges from 0.29 to 0.51; Figure 11a). Extreme runup values per trial are smaller during the last stages of the examined interval (T20–T26) than the $R_{u2\%}$ during berm lowering (T12–T19). The higher energy cluster is segmented and denoted with a red circle (Figure 11a). The berm distortion resulted in offshore sediment deposition and a more dissipative slope across the swash zone, impeding incident waves from reaching the landward section of the beach profile and restricting uprush from impacting the dune toe. Smaller wave heights (H_{m0} < 0.7 m) and shorter wavelengths at the preliminary stages of the experiment (T01–T11) and during the truncation of the berm slope resulted in 0.6–0.8 m $R_{u2\%}$ heights with values exceeding 0.9 m at instances. The maximum runup values were observed during the lowering of the berm crest and until the complete berm erosion when the water depths were 2.14 < h < 2.20 m and the spectral significant wave heights were between 0.7 and 0.8 m.

Figure 11b demonstrates the influence of the berm and beach slope relative to runup. The surf similarity parameter, $\xi_{m-1,0}$, is less than 1.5 and is associated with breaking waves. The relative wave runup, $R_{u2\%}/H_{m0}$, increases linearly with $\xi_{m-1,0}$. Correlation coefficient estimates were in the range of 0.66 and 0.87, implying moderate-to-strong relations between $R_{u2\%}/H_{m0}$ and $\xi_{m-1,0}$. During the erosion of the berm front, the relative runup was less than 2.4 most of the time. $R_{u2\%}/H_{m0}$ values exceeded three only when the water depths were between 2.12 and 2.15 m. However, more dissipative slopes did not lead to greater relative runup heights. Offshore morphological changes led to wave breaking, wave dissipation, and weaker uprush from impacting the dune foot. Three time-series

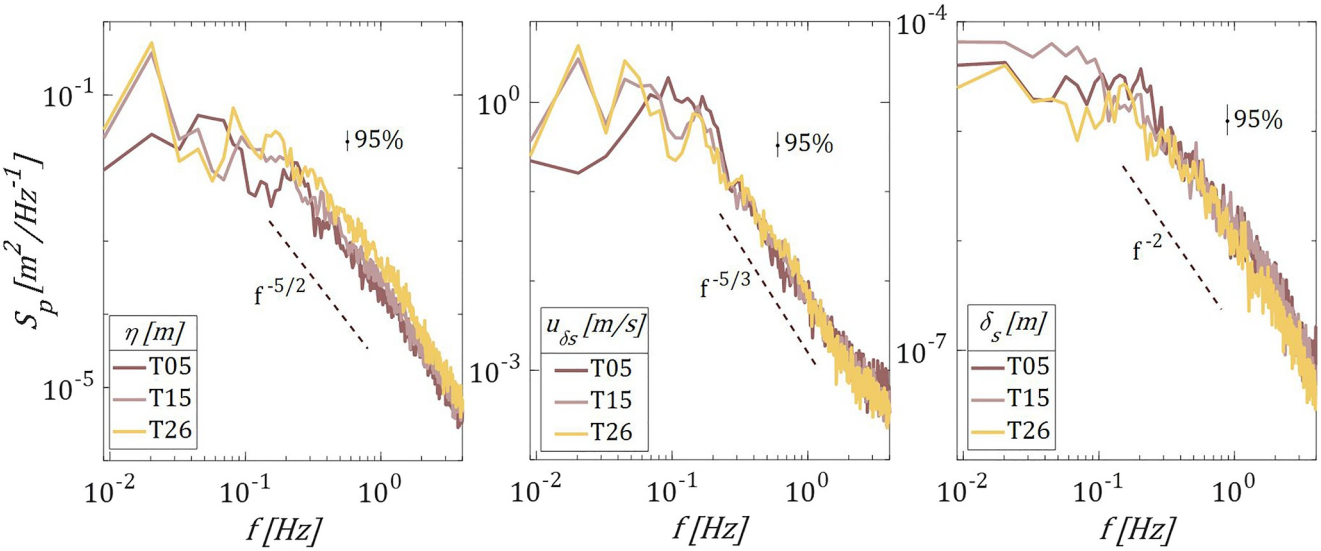

Figure 12. Examples of spectral densities, S_p, of free surface elevations, η (a), flow velocities 1 mm above the top of the sheet layer, $u_{\delta s}$ (b), and sheet layer thicknesses, δ_s (c), with the 95% confidence limits and approximate energy roll-off slopes denoted.

excerpts (Figure 11c) demonstrate the wave runup time series and swash depths in the berm region. Uprush approached the berm crest, but the flow did not overtop the berm during T05 (Figure 11c—1). Overtopping is shown in Figure 11c—2, 3. During trial 26, infragravity motions are noticeable, but despite the subsequent larger swash depths in the berm region, uprush motions hardly reach the dune foot, x = 75.5 m.

3.7. Spectra Analysis

Spectral analysis was performed to define the energy density and its variability during three characteristic trials during the initiation of berm evolution and the truncation of the berm foreshore (T05), wave overtopping (T15), and the complete berm erosion during maximum forcing conditions (T26). Spectral analysis of data collected in the landward swash zone was not possible due to temporal discontinuities. Spectra were calculated at the berm seaward slope where the forcing conditions translated progressively from mid-swash (T05) to an inner-surf zone (T26) state. After detrending the signals, an 8192-point Hamming-tapered window with 50% overlap was used. The resulting spectra were band-averaged over three adjacent frequency bins leaving 20 degrees of freedom. High-frequency motions (>4 Hz) likely due to noise are not of interest and are not displayed.

Free surface elevation (Figure 12a), flow velocity (Figure 12b), and sheet layer thickness (Figure 12c) energy density spectra are presented. The dominant peaks in the free surface spectra are identified between 8 s (0.125 Hz) and 60 s (0.017 Hz). These values correspond to the offshore incident spectral peak periods examined in each trial (Tables 1 and 2) and they are associated with the lower frequencies in the free surface elevation records. The spectra of flow velocities 1 mm above the top of the sheet layer demonstrate similar patterns with spectral peaks noticed near the incident band border and the low-frequency band. The most energetic waves and flow velocities occurred in the low-frequency bands between 0.02 and 0.2 Hz. Free surface elevation energy densities increase with increasing forcing conditions, whereas flow velocities and sheet layer thickness do not demonstrate similar patterns. T26 near-bed flow velocity energy is lower than T05 flow energy densities during short-period hydrodynamics ($f \in [1, 4]$ Hz) and at frequencies corresponding to the peak periods, around 0.2 Hz. Similarly, sheet layer thickness energy densities were greater during earlier trials without prominent peaks over the frequency bands. Spectra peaks are broadly distributed over the low frequencies (0.02–0.15 Hz) of the three examined parameters. Lines proportional to $f^{-5/2}$, $f^{-5/3}$, and f^{-2} were arranged approximately parallel to the saturated zone of wave, velocity, and sheet layer thickness spectra, respectively. The $f^{-5/2}$ roll-off is larger than that reported in previous studies (f^{-4}, Hughes et al., 2014), likely because of the smaller amplitude waves in the present experiment than in the field. The velocity energy roll-off slope follows the −5/3 power law established by Kolmogorov (1962) and Taylor (1938). A f^{-2} roll-off has been reported previously for bed levels in the inner surf and swash zone (Puleo et al., 2014).

4. Discussion

Results from this study illustrate the time-dependent berm response to a scaled storm event, highlighting the contribution of sheet flow dynamics on morphodynamics. The offshore berm migration owing to varying intensities in hydrodynamics is characterized by wave runup and overtopping along with complex near-bed mechanisms of sediment transport. After the truncation of the berm seaward slope, sand was transported onshore to the lee side of the berm by overtopping processes. Mizuguchi and Seki (2015) documented that wave action on the berm slope led to berm erosion. That study lacked detailed measurements of the near-bed hydrodynamics and the impact of swash flow on accretion patterns. Here, it was shown that offshore-directed sediment transport prevailed during the beach profile distortion. This is congruent with previous findings on berm erosion during a storm (Brutsché et al., 2015; Katoh & Yanagishima, 2015). However, this finding differs from field data on dissipative beaches during milder conditions where the berms were already submerged at the beginning of the survey (Houser & Greenwood, 2007).

Temporal variability in berm erosion was examined after classifying three erosive stages: the truncation of the foreshore slope under swash conditions, the lowering of the berm crest during overtopping, and complete berm erosion during rising total water levels. The analysis supports the hypothesis that berm erosion is determined by processes occurring during rising water levels and runup across the swash zone where the sheet flow dynamics dominate sediment mobility. The study demonstrates that a berm on a reflective beach is more likely to experience severe erosion during the first stage of a storm before the maximum waves and water levels impact the back beach. Within 310 min (T01–T15), the sand in the berm region migrated offshore, forming two sand bars. This time interval corresponds to about 9 hours of actual storm-induced hydrodynamics in the field. The time scales were commensurate with those registered by Mizuguchi and Seki (2015) for berm erosion in a surge-dominated coast, whereas extended time intervals were identified in studies that described berm profile changes not associated with extreme events (Katoh & Yanagishima, 2015; Kobayashi et al., 2009). Rapid berm migration as observed in this study may manifest on energetic coastlines in the absence of offshore sediment features (Beuzen et al., 2019). Thus, wave energy dissipation is focused near the berm and leads to deformation. Subsequently, the formation of the two sand bars minimized wave action reaching the backshore area even during increased water levels and wave heights (Figure 5).

This study quantified previously unreported intra-event sheet flow sediment transport rates and near-bed hydrodynamics during berm erosion. The sheet layer thickness and the SFSC did not increase with the rising water levels and larger waves as was previously observed seaward of the surf zone (Dohmen-Janssen & Hanes, 2005). Similar to instantaneous bed-level changes, sheet flow layer thickness and sediment fluxes were greater between the seaward and mid-swash zones owing to shallower depths and the increased shear stresses. Estimated sediment fluxes were offshore-directed commensurate with the observed erosion. On the contrary, in the landward swash zone, onshore-directed sediment transport prevailed throughout most of the experiment, while the dominant net sediment transport direction in the inner-surf zone was offshore. The investigation of cross-shore sediment transport partitioning was beyond the scope of this study. Further research is required to determine the impact of suspended sediment transport on berm dynamics.

Near-bed velocity profiles and sediment concentration profiles in the sheet flow layer are not available from previous storm-related studies because of the lack of measurement capability and the logistical challenges during extreme events. A large data set on sheet flow sediment fluxes was estimated from highly resolved in situ data. Nevertheless, near bed velocities were not always available. The sensors were fixed in the vertical position during the trials under background bed-level variations. Data were lost if the sensors were covered by sand, in case of sediment deposition, too far above the sheet layer in the case of erosion, and/or when water depths were below the sensor measurement elevation. Consequently, the reliability of the approximated cumulative sediment transport rates may have been impacted by these unavoidable gaps in swash zone time series that cannot be interpolated.

While this study provides a deeper understanding of the mechanisms driving berm erosion and sheet flow dynamics, parameters such as pore pressures, flow acceleration, and turbulence were not explicitly investigated. Large pressure gradients can result in upward seepage velocities in the sand layer and enhance bed load transport across the inner-surf zone (Anderson et al., 2017). Sheet flow dynamics may also depend on bore-induced and bed-generated turbulence causing near bed velocity fluctuations and enhanced stresses (Osborne & Rooker, 1999).

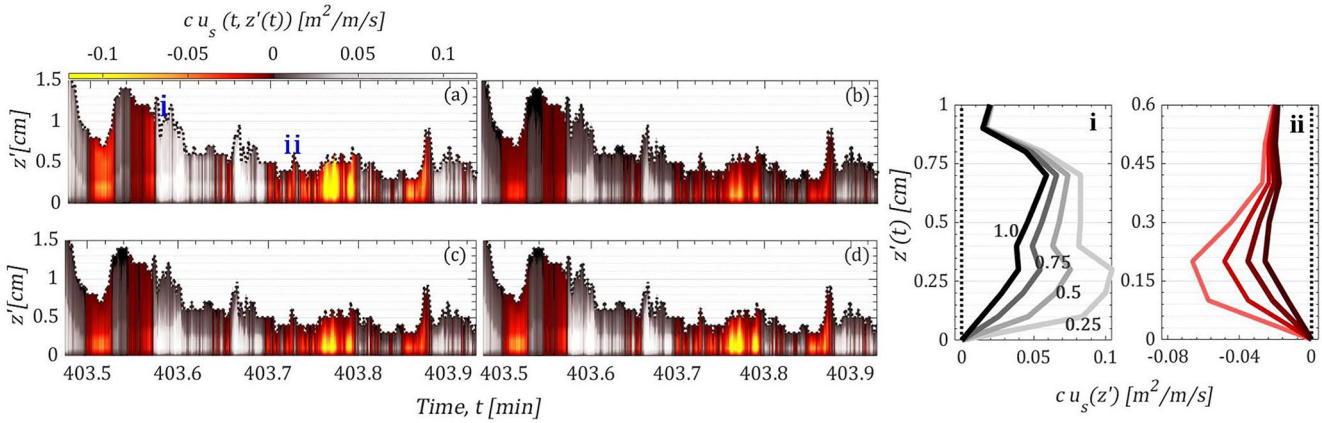

Figure 13. Sheet layer sediment fluxes after varying exponent k in the formula estimating sheet flow velocities (Equation B3). Example sediment flux time series using (a) $k = 0.25$, and the differences between results calculated with (b) $k = 0.5$ and $k = 0.25$, (c) $k = 0.75$ and $k = 0.25$, and (d) $k = 1.0$ and $k = 0.25$. Comparison of inner surf sediment flux profiles (magnitudes and directions) approximated using various k exponents are presented at two instances of time (i, ii) that are indicated with the relevant green triangles in panel (a). Gray colors imply onshore-directed sediment transport (i). Red colors denote offshore-directed sediment transport (ii).

These aspects warrant further investigation of sheet flow processes (Bond et al., 2023) to advance our understanding of nearshore morphodynamics.

To the authors' knowledge, an instrument capable of quantifying sheet layer velocity profiles in the swash zone does not exist. Sheet flow velocity profiles were related to the flow field adjacent to the top layer of sheet flow (Equation B3, Appendix B5). The exponent, $k = 0.62$, was initially suggested for sediment particle velocity profiles in the swash zone (Puleo et al., 2017), and $k = 0.75$–1.0 was applied to compute sheet layer velocities in uniform and oscillatory flow (Sumer et al., 1996; Wilson, 1966). An exponent, $k = 0.5$, was selected to evaluate inner-surf and swash zone sheet flows in this study. The value conforms to results from surf zone non-breaking wave conditions (Y. H. Wang & Yu, 2007) and the 95% confidence limits on the exponent, $k \in [0.47, 0.76]$, as documented by Puleo et al. (2017). The impact of the previously suggested exponents on sheet flow layer sediment fluxes was explored (Figure 13). Sheet flow sediment fluxes decrease with greater k values since the k value controls the velocity decay into the sheet. Altering the exponent from 0.25 to 0.5 diminished the fluxes by ~6%, whereas changing k from 0.25 to 0.75 decreased the flux magnitude by ~68%. It is noticeable that the flux differences between the results obtained from $k = 1.0$ and $k = 0.25$ are almost equal to the magnitudes resulting from $k = 0.25$. Using these modified k values alters the cumulative fluxes presented in Figure 10 and yields R^2 values of 0.37 for $k = 0.25$ and 0.12 for $k = 1.0$.

Prior research (Suzuki et al., 2007; van der Zanden et al., 2015) evaluated cross-shore sediment transport rates using time-sequenced beach profile data in the absence of direct sediment flux estimates. Here, a large data set of bed-level elevations and continuity inversion estimates of total sediment transport were used to investigate sheet flow sediment transport per trial. However, the approximation of total sediment transport rates was intricate. The initial inverse application of the continuity equation led to bias on the profile boundaries, which was also observed in prior studies (Jensen et al., 2009; van der Zanden et al., 2015). A Monte Carlo simulation was used (§3.5) to randomly minimize measurement uncertainties and measurement limitations, for example, lack of porosity data. The comparison between the total sediment transport rates derived from in situ measurements and the rates estimated using morphology data indicates that the results are directionally consistent and of the same order of magnitude. The sediment transport analysis was carried out applying the averaging approach to continuity inversion to generate new q_M values. Greater q_M fluxes compared to q_R fluxes were found at ST2 and ST3, and smaller values were found for ST1. Consequently, the coefficient of determination ($R^2 = 0.14$) from this regression was found to be smaller than the coefficient estimated between the Monte Carlo-derived fluxes and the recorded data ($R^2 = 0.31$; Figure 10).

5. Conclusions

The controls of berm erosion during storm events are diverse and complicated. A laboratory experiment was conducted on a near-prototype beach profile yielding the following conclusions:

1. Runup and infragravity motions were responsible for the most prominent berm volumetric losses, although some sediments were transported upslope by the uprush leading edges.
2. Three key morphological changes stemmed from berm erosion: (a) sediments removed from the berm initially accreted near the berm toe creating shallower bathymetry (b) the eroded sand was later deposited in the surf zone generating two sandbars that helped attenuate subsequent wave energy (c) sediments were deposited at the lee side of the berm throughout wave overtopping, steepening the backshore. The formation of these morphologic features delayed the continuously increasing wave intensity from reaching the backshore, preventing sand losses at the dune toe.
3. Net cross-shore sediment transport was predominately offshore-directed. Sheet flow layer sediment fluxes may dominate over suspended sediment fluxes in the swash zone owing to the shallower water depths and larger bed shear stresses.
4. Swash zone bed-level changes were more energetic than the bed-level changes in the surf zone. Low-frequency motions had the most impact on mid- to landward-swash bed-level variations.
5. Energy densities in sheet flow dynamics were larger during swash zone processes. Early storm stage morphodynamics in the swash zone could be critically important to erosive processes as wave intensity increases during a storm event.

This study highlights the significance of sheet flow on swash zone and berm sediment transport dynamics and documents the contribution of sheet flow sediment fluxes. Overall, essential progress in modeling storm-driven berm erosion requires the incorporation of near-bed hydrodynamic and morphodynamic processes across the swash zone. The presented data set can support future numerical simulations of berm evolution and enlighten nearshore morphodynamics.

Appendix A: Instrumentation

Two acquisition systems were used to record data from in situ sensors, referred to as DAQ and UD. Each system received time corrections from a Global Positioning System antenna. DAQ was synchronized with the wavemaker signal at 100 Hz. UD and DAQ both recorded a signal allied to the wave paddle movement. Cross-correlation of these signals from the two systems enabled synchronization of any small time offsets for the UD records. All measurements were obtained in flume coordinates with an origin at the flume bottom and right side (observer looking onshore) of the wave paddle neutral position ($x = 0$, $y = 0$, $z = 0$) with a positive landward (x) and upward (z) direction. Spanwise coordinates (y) increased to the left (right-handed coordinate system). More than 70 sensors were deployed (Figure A1), but only sensors pertinent to this paper are described herein.

Fourteen capacitance wave gauges (WGs) with 100 Hz sampling frequency were placed along the flume wall to measure offshore water surface elevations and wave propagation. A WG was placed at the berm foot, where the wave properties were expected to alter due to the substantial slope transformation. The rest of the WGs were located offshore with a typically 3.5 m cross-shore spacing. Wave gauges near $x = 35$ m, where greater wave transformation was expected, had smaller cross-shore separation distances. Swash depths and instantaneous bed levels shoreward of the initial berm foot were measured with ultrasonic distance meters (UDMs) (Baldock, 2009; Turner et al., 2008). These non-intrusive instruments emit acoustic signals to define the distance between the sensor and the variable sand or water surface with accuracy O(1 mm) (Russell et al., 2009). Seven UDMs (32 Hz sample rate) were deployed from the flume side wall higher than 1.2 m above the sand bed. The typical cross-shore spacing was 1.3 m.

Four acoustic Doppler profiling velocimeters (ADPVs; Nortek Vectrino II; Craig et al., 2011) were deployed in the vicinity of the berm to record near-bed streamwise (u), spanwise (v), and vertical (w) velocities. Acoustic Doppler profiling velocimeter (ADPV) measurement accuracy is ±1% of the measured value, ±1 mm/s (NORTEK, 2017). Each ADPV was attached to a vertical metal pipe stabilized on a beam hanging from the flume wall. ADPVs were placed 1.3 m from the side wall to minimize interference and allow a surveying platform to move unhindered along the flume centerline. The cross-shore instrument stations were located 3.65 m apart to reduce flow modification by the deployment structures. All ADPVs were oriented downwards with the central transmitter 0.055 m above the initial bed and sampled at 100 Hz. The measurement range was 0.04–0.07 m yielding an initial velocity profile that intersected the bed. The flow field was highly resolved in the vertical direction with 30 bins separated by 0.001 m. Additionally, the ADPVs were set to record the bottom distance acoustic profile at 10 Hz.

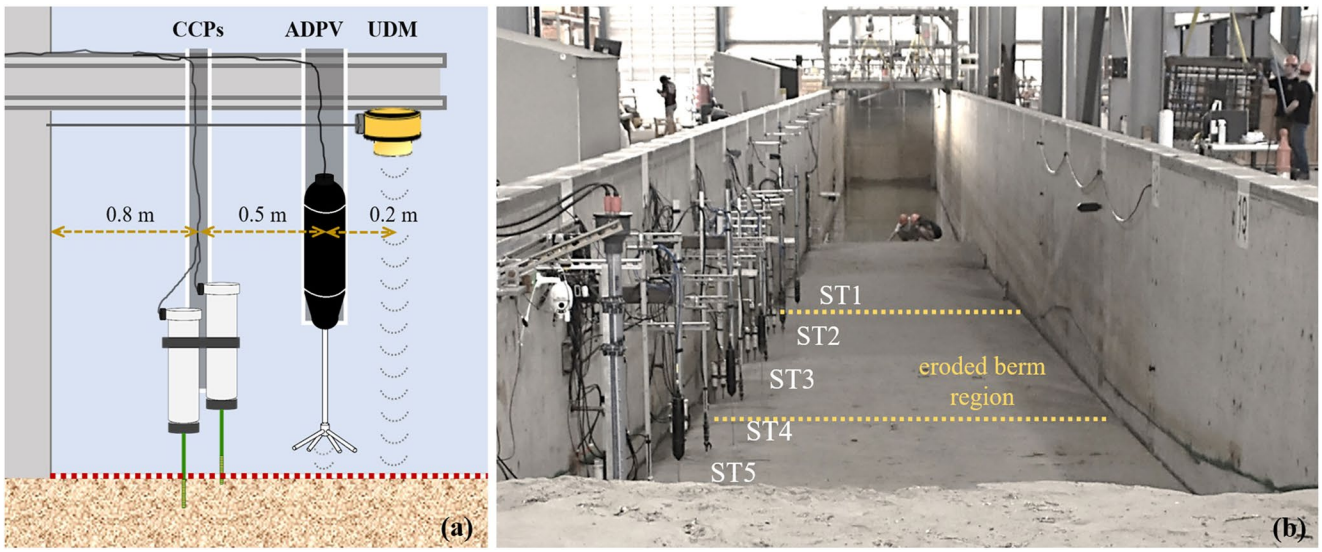

Figure A1. Schematic of sensor deployment at a station—not to scale (a). The view of the instrumentation in the large wave flume and the beach profile after the berm eroded (b).

Sheet flow sediment concentrations were sampled with conductivity concentration profilers (CCPs, Lanckriet et al., 2013; Puleo et al., 2010). CCPs collected instantaneous electrical conductivities over a profile of 0.029 m with 0.001 m resolution, 0.003 m accuracy, and 8 Hz sampling frequency. The records were translated into sediment concentrations with a calibration formula that expresses the conductivities in the two-phase mixture as volume fractions (Archie, 1942). Two CCPs were deployed offshore, at $x = 51$ m, one to quantify the conductivity of the saturated packed bed and the other to measure the conductivity of "sediment-free" water. Eight CCPs were installed at the same cross-shore locations as the ADPVs for estimating sediment flux. Moreover, CCPs were placed in pairs to extend the vertical range. Sensors in each pair were spaced 0.07 m apart in the spanwise direction. All probes were pointed downwards and parallel to the streamwise direction. The vertical offset between the probes was 0.026 m and the higher probe was initially placed 0.03 m in the sand. Only the measurement sections of the probes ($1.6 \times 5.6 \times 40$ mm) were inserted into the sand to minimize scouring effects and facilitate the vertical adjustment of the sensors after each trial. CCPs were also used to track changes in bed elevations during the trials (Lanckriet et al., 2014; Puleo et al., 2014).

A light detection and ranging (lidar) terrestrial laser scanner (RIEGL LMS-Z390i) was installed on the surveying platform 7 m offshore of the berm crest to quantify morphodynamics. The lidar was set to function in the line scan mode (2 scans/s) to the sample at high frequency (up to 8,000 points/s) a cross-shore transect (x, z) with $\pm$0.006 m accuracy and 0.001° vertical angle resolution. Laser scans were obtained between the shoreline and the lee side of the dune. Records of the water surface and bed elevations yielded runup levels (Bond et al., 2023). Four Multiple Transducer Arrays (MTA; SeaTek; Jetté & Hanes, 1997), each of which consisted of eight sonar transducers, were installed under the platform. The relative distance between the transducers was 0.065 m. The array traversed the subaqueous portion of the beach producing a profile with elevation accuracy of $\pm$0.02 m.

Appendix B: Data Analysis

B1. Morphology

Remote-sensing techniques were used to track berm erosion and bathymetry progression. Approximately 60 laser scans of the flume centerline transect were collected in the last 30 s of each trial. These scans were merged and georeferenced from the lidar coordinate system to the wave flume coordinate system using known control points. Subsequently, a plane rectification method (O'Dea et al., 2019) was applied and the profiles were aligned to a

baseline scan to consider the effects of the shifting lidar position on the measurements. Swash depths were eliminated from the bed elevations with the use of a 25 s moving minimum filter in time (Bond et al., 2023).

Anomalies in the lidar and MTA data sets were mostly present close to the waterline owing to the insufficient depth for the MTA and the inability of the laser to penetrate water. Erroneous MTA point records were eliminated. Additionally, data at given cross-shore locations outside 2 standard deviations from the mean were removed. The MTA records were then averaged alongshore. The bathymetry was linearly interpolated to 5 mm cross-shore intervals to be consistent with the high-resolution laser line scans. The quality-controlled elevation and bathymetry records were conjoined approximately 60 m from the wavemaker, where the water depth was shallower than 0.3 m, to generate beach profiles. Berm morphological progression was obtained after each trial during the first 590 min (T01–T26) of the physical model simulations across the region from the berm toe at x = 59 m to the landward end of the berm lee side at x = 75 m.

B2. Free-Water Surface and Bed Elevations

Different sensors were capable of capturing the bed evolution and water surface elevations. Raw UDM records were converted to bed levels relative to the pre-trial elevation after applying a two-sigma filter and a moving minimum function. Swash events were segregated from the bed levels with a conditional function that specified local maxima by comparing neighboring samples and the durations of uprush and backwash motions. Local peaks were the sensor readings representing the highest water level during a swash event. In the region of frequent bore collapse, water droplets and residual foam could obstruct the acoustic signal. Samples obtained during these intervals from UDM1 were rejected and replaced with data received by the WG that was located near the ultrasonic sensor offshore of the berm (x = 61.75 m; WG14).

Using acoustic sensors made it possible to quantify bed-level fluctuations and swash events from the berm front, berm crest, and berm landward side. Spatial coarseness in ultrasonic elevation measurements was improved using lidar in line scan mode. Laser scans performed over turbulent and bubbly water surfaces were translated to swash excursions; swash depths were extracted from the rectified lidar records, and the leading edge of uprush motion was defined as the location shoreward of which swash depths were less than 0.02 m (Bond et al., 2023). Instantaneous flow velocities and sediment concentrations were later associated with the collocated UDM time series since the laser scan line was 1.5 m off the sensor stations along the flume centerline. The comparison between bed elevations obtained through UDMs at the end of each trial and lidar samples at the same cross-shore locations exhibited good agreement in the swash region with elevation differences O(0.01 m) and correlation coefficient, R^2, equal to 0.83.

Bed detection by the UDMs and laser scanner was not possible when the sand surface was covered by water. During submerged conditions, bed-level information was retrieved from the CCP data sets following Lanckriet et al. (2013). Concentration profiles yielded bed-level progression and swash events at the berm seaward slope, berm crest, and berm lee side. Temporal data discontinuities were observed over the crest and the lee side of the berm when swash conditions prevailed. Sediment concentrations were not monitored at the landward end of the berm slope, owing to the low-saturated sand at the landward side of the berm since the leading tip of the uprush flows rarely reached the station before T26. Sheet flow concentrations were discerned in the rough range of $0.08 \leq c \leq \sim 0.6$ m^3/m^3. Smaller concentrations were obtained in the lower water column signifying sediments in suspension, whereas greater values $c > \sim 0.6$ m^3/m^3 denote sensor readings in the packed bed.

B3. Near-Bed Velocities

ADPV time series were processed (Figure B1) to detect and discard spurious data from the records using denoising, de-spiking, and other quality control techniques. First, water elevation data were used to identify when the ADPV probes were exposed to air during wave troughs or shallow swash flows. Swash zone velocities could not be captured during shallow water depths (<0.06 m). Successively, data were quality controlled by applying amplitude and correlation tests to all acoustic beams (Voulgaris & Trowbridge, 1998). Bubbles and foam could alter the strength of the return acoustic amplitude, decreasing the measurement quality. Velocities were discarded when the acoustic return signal was lower than −20 dB in any x, y, or z direction. Additionally, velocity estimates were rejected when the normalized amplitudes of the autocorrelation function were less than 55%. Records consisting of not-a-number (NaN) values were excluded from the analysis and the resulting data were despiked

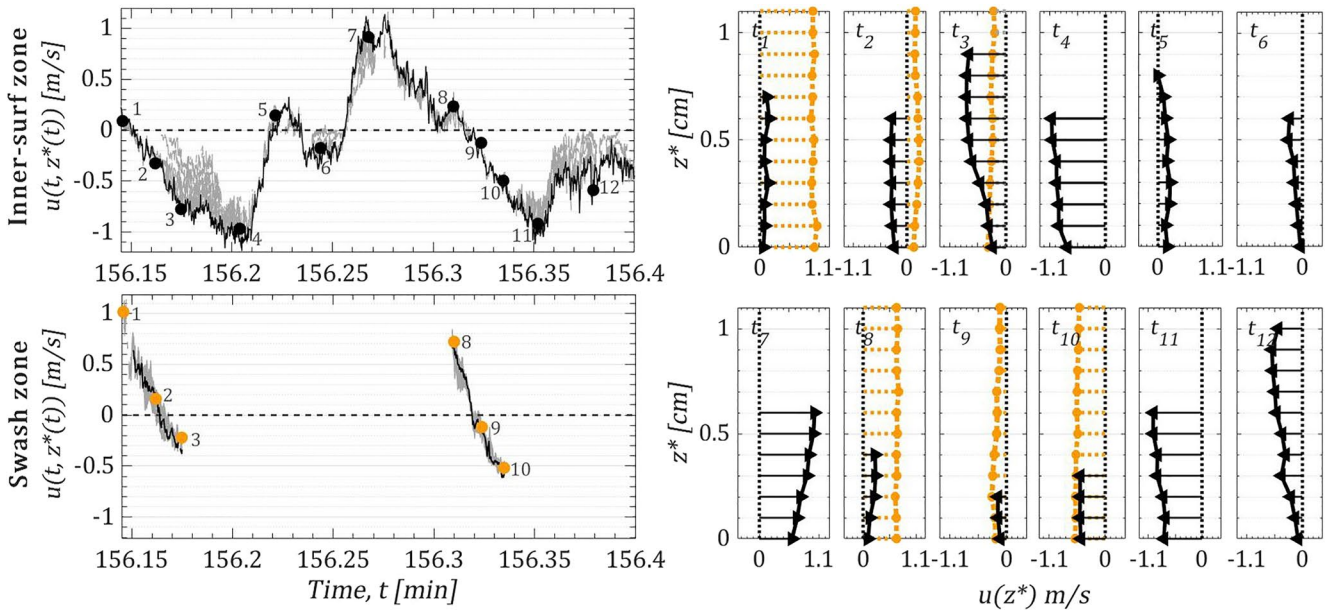

Figure B1. Excerpts of near-bed cross-shore velocity time series collected by multiple acoustic Doppler profiling velocimeter (ADPV) bins in the (a) inner surf and (b) swash zones. Instantaneous inner-surf zone velocity profile data at 12 instances of time (t_1–t_{12}) (solid, colored lines) are compared to the corresponding swash zone velocity profiles (dotted gray lines) (c, d). Profiles were created using the velocity time series collected by ADPV bins that were above the top of the sheet flow layer (gray lines). Black lines represent the velocities measured 1 mm above the top of the sheet layer. Positive values denote onshore-directed flow. Negative values denote offshore-directed flow.

using acceleration thresholding (Goring & Nikora, 2002) and 3D phase space methods (Goring & Nikora, 2002; Mori et al., 2007).

Discarded data were initially replaced with NaN. Inner-surf zone velocities were then interpolated using an autoregressive model to the points enveloping the NaN data gaps. The order of the model depended on the number of retained observations preceding the data gaps. Discontinuities in the denoised swash zone velocities were not interpolated. The percentage of data points discarded and interpolated in the inner-surf zone varied from trial to trial. Note that a substantial portion of this data removal occurred when the sensors were not immersed, corresponding to times when velocity data should not exist.

B4. Concentrations

A single CCP was not always capable of capturing the entire sheet flow layer for long time intervals owing to the finite probe length. Records collected between T01 and T03 were excluded when the low water levels and low sand saturation resulted in poor CCP response. Archie's law (Archie, 1942; Equation B1) was applied to the retained electrical conductivities to convert to volumetric sediment concentrations, c.

Fluid conductivity varies with temperature, requiring fluid conductivity measurements for each trial using the offshore submerged CCP. The exponent m depends on the shape and size of the sediment particles, and it is not impacted by the conductivity of the fluid (Lanckriet et al., 2013). Hence, m was evaluated after quantifying the conductivities in the packed bed where the solid fraction was assumed equal to 0.644 for natural sands (Bagnold, 1966). The volumetric sediment concentration was essentially zero in the upper water column at the beginning of the first trial. These values yielded a calibration factor m equal to 1.48, which is within the range of values $1.39 < m < 1.58$, reported in previous studies on the resistivity of marine sands (Jackson et al., 1978).

$$c = \varphi_s = 1 - p_r = 1 - \left(\frac{\sigma_{sf}}{\sigma_f}\right)^{\frac{1}{m}}, \tag{B1}$$

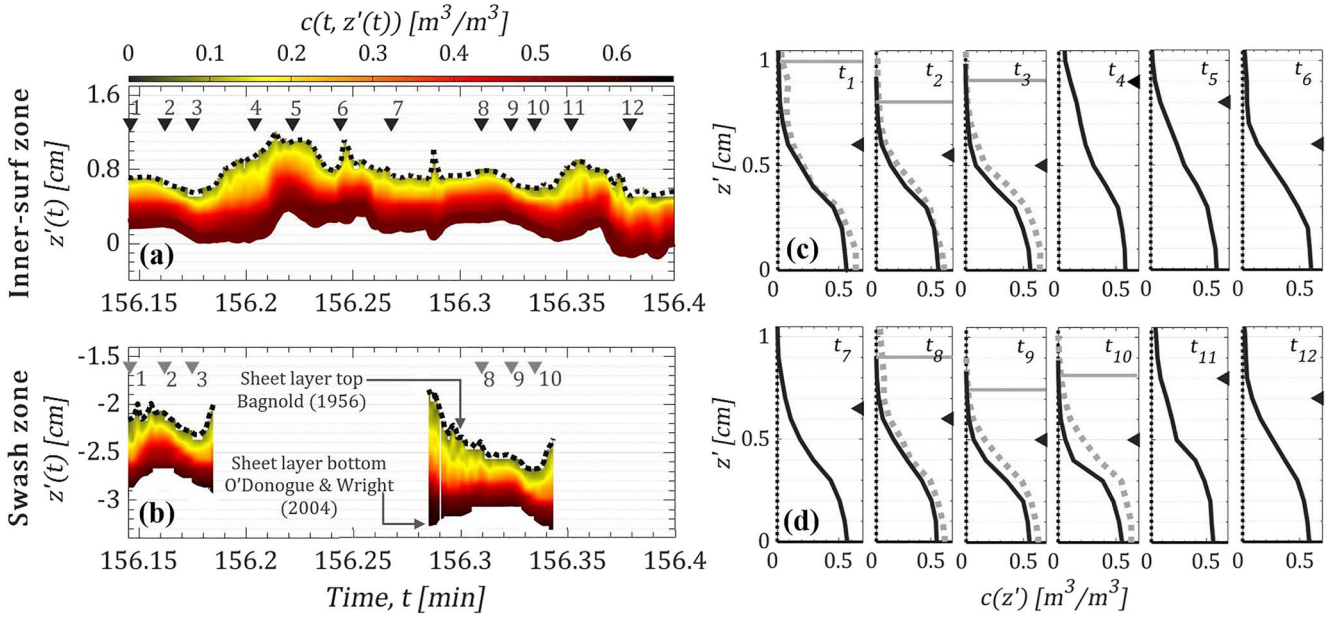

Figure B2. Example time series displaying sheet layer sediment concentrations in the (a) inner surf and (b) swash zones. Sheet flow sediment concentration profiles are displayed for 12 instances of time (t_1–t_{12}) (c, d). Inner-surf zone concentration profiles (solid black lines) and swash zone concentration profiles (dotted gray lines) are displayed. On panels (c, d), the black triangles (t_1–t_{12}) and the gray lines (t_1–t_3, t_8–t_{10}) indicate the top of the sheet layer in the inner surf and swash zones, respectively.

where φ_s is the solids volume fraction (vol%), p_r is the porosity of unconsolidated sand, σ_{sf} is the conductivity of the sediment-fluid mixture, σ_f is the conductivity of the fluid, and m is a calibration factor related to the decrease in electrical conductivity with increasing solid fraction in the mixture.

The top boundary of the sheet layer was discerned as the volumetric concentration contour of 8%, where the grain spacing is approximately equal to the mean sediment diameter (Bagnold, 1956). The bottom of the sheet layer was identified following the O'Donoghue and Wright (2004) approach. Here, the instantaneous sediment concentration profile is fit using an empirical modified power law (Equation B2).

$$c\left(t, z'(t)\right) = c_b \frac{\psi^{\alpha}}{\psi^{\alpha} + \left(z'(t) - z_{b,t}\right)^{\alpha}}, \tag{B2}$$

where, $c(t, z'(t))$ is the sediment concentration in the sheet flow layer at elevation z', where t is the time elapsed from the beginning of the experiment, c_b is the packed bed sediment concentration, α and ψ are free shape parameters related to the slope of the curve and the sheet layer thickness respectively, with $0 < \psi < 0.01$ (m) and $1.10 < \alpha < 3.90$ (–). $z_{b,t}$ is a free parameter that comprises the first approximation of the sheet layer bottom (m) and is defined with a nearest neighbor search where $0.635 < c < 0.655$ (m^3/m^3).

Sheet flow sediment concentration time series (Figures B2a and B2b) and selected profile records (Figures B2c and B2d) from T09 are provided. Two waves and two swash events respectively over ~15 s at the berm seaward slope and berm crest are shown as examples. Temporal gaps identify times between successive swash events. Instantaneous sediment concentrations extend from the bottom of the sheet layer to the higher CCP measuring bin. The sheet layer is dynamic with the erosion depth varying from 0.005 m ($24d_{50}$) to 0.009 m ($43d_{50}$) at the offshore side of the berm. At the berm crest, the erosion depth was greater, exceeding 0.01 m ($48d_{50}$) at times denoting that the sheet flow was more dynamic in the swash zone. These values are proportional to the sheet layer thicknesses presented by Mieras et al. (2017) during overall milder forcing conditions. Moreover, sheet flow expansion/dilation and larger sheet layer thickness led to steeper concentration profiles. When the sheet flow layer diminished, the profiles became linear above the top sheet layer with power-law tails near the bottom. Swash zone sheet flow layers were overall thicker than the sheet flow layer in the inner-surf zone. The 1 mm distance between the probe electrodes resulted in inadequate resolution and smoothing of the concentration profiles in the absence of hydrodynamic forcing and during gradual flow reversals (Lanckriet et al., 2014). Sheet flow layer thickness detected under these conditions was thinner than 5 mm and was removed from the data set.

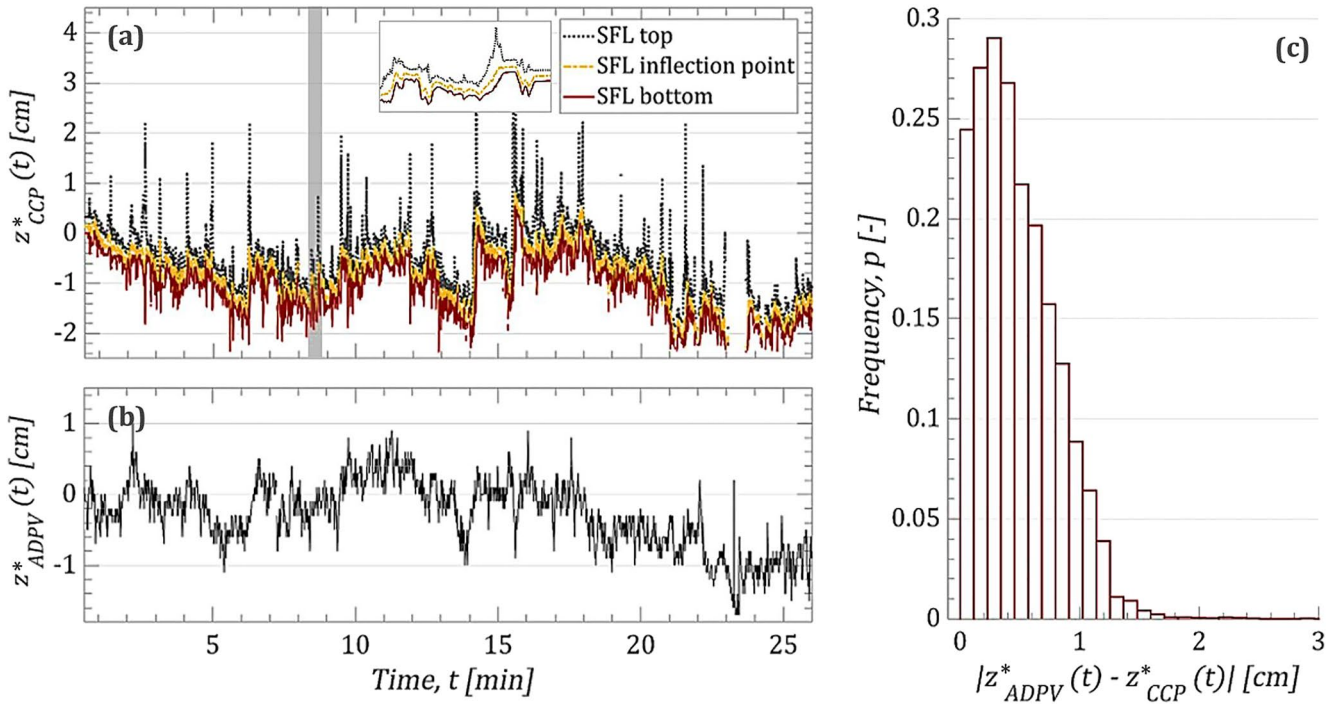

Figure B3. Example time-series and comparative analysis of bed-level data captured by conductivity concentration profilers (CCPs) (a) and acoustic Doppler profiling velocimeter (ADPV) (b). A highlighted segment (8.4–8.8 min, gray panel) provides a detailed examination of sheet flow layers, including the top, inflection point (Mieras et al., 2017), and bottom layers (a). The top of the sheet flow layer monitored by ADPV (b). Histogram depicting the absolute differences between records obtained from CCPs and ADPV.

To establish a better understanding of the bed-level dynamics, a comparative analysis was conducted between CCP bed-level estimates (top of the sheet layer), and ADPV distance measurements, which represent the level of the sand surface (Figure B3). This examination aimed to gauge the degree of correlation between the two data sources across the sensor stations before estimating the corresponding sediment fluxes. Correlation analyses were performed for records acquired at ST1 ($R^2 = 0.21$), ST2 ($R^2 = 0.18$), and ST3 ($R^2 = 0.11$). The low correlation coefficients could be attributed to the different physical mechanisms used to identify the "bed", namely, conductivity and acoustic return amplitude, and the alongshore distance of approximately 0.5 m between the sensor locations.

B5. Velocities in the Sheet Layer

An example of cross-shore velocities from $x = 65$ m during two swash events (Figure B4c) indicates differences from the respective inner-surf zone time series at the berm seaward slope (Figure B4a). The 10 MHz ADPV acoustic signal cannot reliably penetrate the sheet layer and any velocities returned below the top boundary of the sheet later were rejected. Velocities in the sheet layer require estimation. Previous research suggested semi-empirical formulas for the velocity decrease from the top of the sheet layer (Soulsby & Damgaard, 2005; Sumer et al., 1996). Y. H. Wang and Yu (2007) combined these formulas and applied a profile shape parameter, k, equal to 0.5, to quantify the shape of the velocity profile in the sheet layer as

$$u_s\left(t, z'(t)\right) = u_{\delta s}(t)\left(\frac{z'(t)}{\delta_s(t)}\right)^k, \tag{B3}$$

where u_s is the fluid velocity in the sheet layer and $u_{\delta s}$ is the fluid velocity 1 mm above the top of the sheet layer. k is an empirical exponent that was set equal to 0.5 (Puleo et al., 2017; Y. H. Wang & Yu, 2007; Wilson, 1966), and δ_s is the sheet layer thickness defined as the vertical distance between the bottom and top boundary of the sheet layer, $\delta_s = z^* - z'$.

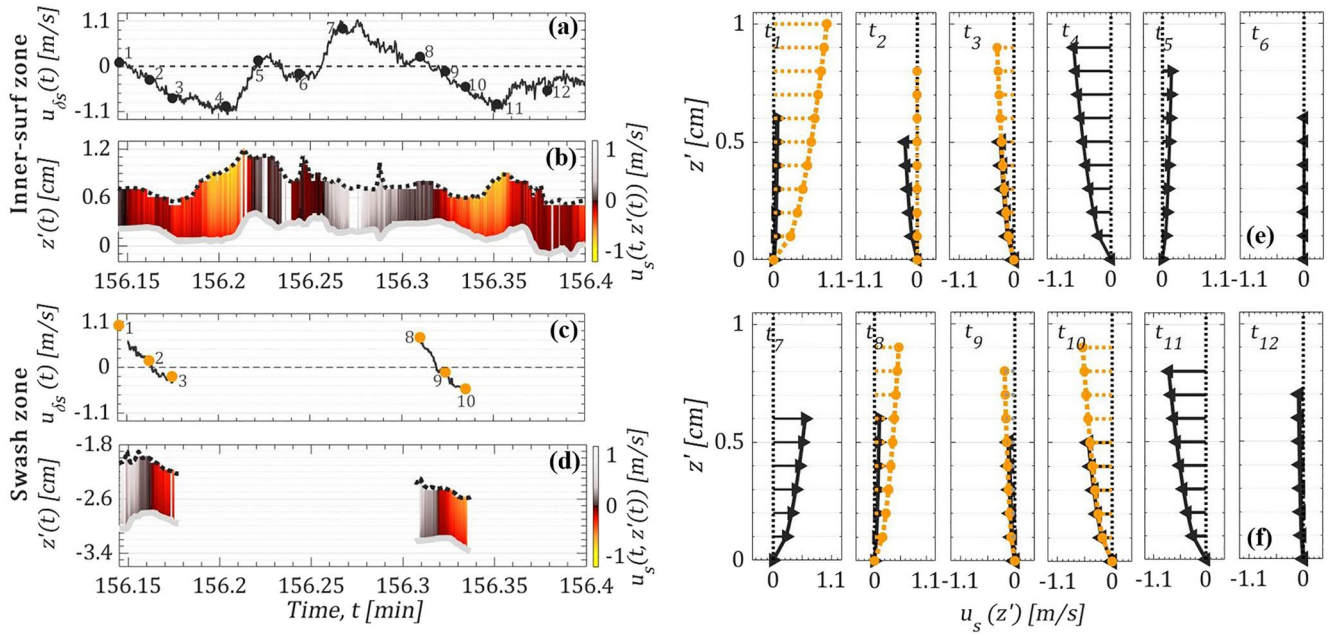

Figure B4. Excerpts of cross-shore velocity time series from acoustic Doppler profiling velocimeter bin 1 mm above the top of sheet layer (a, c) and sheet flow velocity time-space segments (b, d) in the inner surf (a, b) and swash (c, d) zones evaluated with Equation B3. Instantaneous inner surf zone velocity profiles (solid black lines) at 12 selected time instances (t_1–t_{12}) (e, f) are compared to the corresponding swash zone velocities (dotted orange lines) (e, f). Positive values denote onshore-directed flow. Negative values denote offshore-directed flow.

The top of the sheet layer was identified using the ADPV center beam amplitude when the water depth was sufficient to submerge the probe. Otherwise, the CCP was used to define the top of the sheet layer at the 8% volumetric concentration. A video-based approach for sediment particle velocities in the swash zone of a laboratory setting verified Equation B3 finding k equal to 0.62 with a 95% confidence interval of 0.47–0.76 (Puleo et al., 2017). Sheet flow velocities computed at various time instances are juxtaposed with near-bed velocities and show how the sheet layer responds to the hydrodynamic forcing (Figure B4). The velocity time series is from the 20th ADPV bin that was close to the surface of the mobile bed but remained above the top of the sheet layer during the examined time interval. During this excerpt, uprush peak $u_{\delta s}$ is 1.02 m/s at 156.13 min, while the maximum inner surf onshore directed $u_{\delta s}$ exceeds 1.1 m/s at 156.28 min. In the inner-surf zone, sheet flow thickness was amplified under the maximum offshore-directed flow velocities. The sheet flow layer responded quasi-steadily to maximum backwash velocities and there was a slight lag between the onshore-directed velocities and the sheet layer fluctuations, likely because of the influence of the turbulent mixing on the sediment grain motion. Swash sheet flow thickness increased during uprush and backwash motions with the uprush leading to sheet flow thicknesses that could be at least 30% larger than those in the inner-surf zone in some instances.

Notation

c	sheet flow sediment concentrations (m^3/m^3)
d_{50}	median sediment diameter (mm)
E	uncertainty associated with an error source (m)
h	water depth measured at x = 14 m, from the flume bottom to the free-water surface (m)
h^*	water depth measured from the sheet flow layer top (m)
H_{m0}	spectral significant wave height (m)
H_o	offshore wave height (m)
H_s	significant wave height (m)
k	empirical exponent used in Equation B3 (–)
L_o	offshore wavelength (m)
m	calibration factor in Equation B1 (m)
n_{d50}	sediment size scale (–)

n_h	depth scale (–)
n_l	length scale (–)
n_{s-1}	relative density scale (–)
n_{Tm}	morphological time scale (–)
N_w	number of waves generated per trial (–)
p	probability of occurrence (%)
p_r	porosity of the medium (–)
q	sheet flow sediment transport rates ($m^2/m/s$)
q_M	morphology-estimated total sediment transport rates (m^2/s)
q_R	total sediment transport rates derived from in situ records (m^2/s)
q_t	total sediment transport rates at cross-shore location x (m^2/s)
$R_{u2\%}$	2% runup exceedance level (m)
$s_{m-1,0}$	wave steepness related to offshore wave spectral parameters (–)
S_p	spectral density (m^2/Hz^{-1})
$T_{m-1,0}$	spectral wave period (s)
T_p	peak period (s)
u_s	sheet flow velocity (m/s)
$u_{\delta s}$	flow velocity 1 mm above the top of sheet layer (m/s)
V_{fr}	volume fraction (%)
Y	maximum elevation deviation (m)
z	elevation measured from the origin of the flume coordinate system
z'	elevation from the bottom of sheet flow, with $z'(t) = z'(t) - z'(t = 0)$ (m)
z^*	elevation from the top of sheet flow, with $z^*(t) = z^*(t) - z^*(t = 0)$ (m)
$z_{b,t}$	free parameter that comprises the first approximation of the sheet layer bottom in Equation B2 (m)
α	free shape parameter in Equation B2 (–)
β	berm slope angle (°)
δ_s	sheet layer thickness (m)
η	free surface elevation (m)
μ	mean value of probability distribution (m)
$\xi_{m-1,0}$	surf similarity parameter (–)
ρ_s	sediment density (kg/m^3)
ρ_w	freshwater density (kg/m^3)
σ	standard deviation of probability distribution
σ_f	conductivity of the fluid (S/m)
σ_{sf}	conductivity of the sediment-fluid mixture (S/m)
φ_s	solids volume fraction (vol%)
ψ	free shape parameter in Equation B2 (m)

Acknowledgments
This work was supported by the National Science Foundation (NSF) under Grant 1519679, 1756714, 1756477, and 1756449. Special thanks to Pedro Lomonaco and Tim Maddux at the O.H. Hinsdale Wave Research Laboratory, Oregon State University, for their diligent contributions to this project, and all the insightful discussions. The authors would like to thank the following researchers/visitors for their help during the experiment: Acevedo I., Cargill S., Converse J., Do K., Figlus J., Garrey N., Innocenti R., Kaneko A., Larner M., Lee D., Lee E., Lee S.-B., Lewis R.-E., Moragues M.-V., Rafati Y., Rumaker K., Shin S., Smith J, Suzuki T., and Tsai B. The authors thank the three reviewers for comments that improved clarity and reduced the length of this paper.

Data Availability Statement

Data from the DUNE3 experiment are available through DesignSafe-CI, project number 2145 (Pontiki & Puleo, 2022, https://doi.org/10.17603/ds2-csmw-8x65; Bond & Wengrove, 2022, https://doi.org/10.17603/ds2-nf3k-fe18).

References

Anderson, D., Cox, D. T., Mieras, R., Puleo, J. A., & Hsu, T.-J. (2017). Large-scale laboratory observations of pore-pressure gradients on a surf-zone sand bar. *Journal of Geophysical Research: Oceans*, *122*(6), 5169–5193. https://doi.org/10.1002/2016JC012557

Archie, G. (1942). The electrical resistivity log as an aid in determining some reservoir characteristics. *Institute of Mining and Metallurgical Transactions*, *14*(01), 54–62. https://doi.org/10.2118/942054-G

Bagnold, R. A. (1956). The flow of cohesionless grains in fluids. *Proceedings of the Royal Society of London*, *249*(964), 235–297. https://doi.org/10.1098/rsta.1956.0020

Bagnold, R. A. (1966). The shearing and dilatation of dry sand and the "singing" mechanism. *Philosophical Transactions of the Royal Society of London - Series A: Mathematical and Physical Sciences*, *295*(1442), 219–232. https://doi.org/10.1098/rspa.1966.0236

Baldock, T. E. (2009). Discussion of "measurement of wave-by-wave bed-levels in the swash zone" by Ian L. Turner, Paul E. Russell, Tony Butt [Coastal Eng. 55 (2008) 1237-1242]. *Coastal Engineering*, *56*(3), 380–381. https://doi.org/10.1016/j.coastaleng.2008.12.002

Bates, K. T., Savage, R., Pataky, T. C., Morse, S. A., Webster, E., Falkingham, P. L., et al. (2013). Does footprint depth correlate with foot motion and pressure? *Journal of the Royal Society Interface*, *10*(83), 20130009. https://doi.org/10.1098/rsif.2013.0009

Beuzen, T., Harley, M. D., Splinter, K. D., & Turner, I. L. (2019). Controls of variability in berm and dune storm erosion. *Journal of Geophysical Research: Earth Surface*, *124*(11), 2647–2665. https://doi.org/10.1029/2019JF005184

Bond, H., & Wengrove, M. (2022). Dune subsurface hydrodynamics during an extreme event, in physics of dune erosion during extreme surge and wave events [Dataset]. DesignSafe-CI. https://doi.org/10.17603/ds2-nf3k-fe18

Bond, H., Wengrove, M., Puleo, J. A., Pontiki, M., Evans, M., Feagin, R. A., & Huff, T. (2023). Beach and dune subsurface hydrodynamics and their influence on the formation of dune scarps. *Journal of Geophysical Research: Earth Surface*. Under Review.

Bouws, E., Günther, H., Rosenthal, W., & Vincent, C. L. (1985). Similarity of the wind wave spectrum in finite depth water: 1. Spectral form. *Journal of Geophysical Research*, *90*(C1), 975–986. https://doi.org/10.1029/JC090iC01p00975

Brutsché, K. E., Wang, P., Rosati, J. D., & Beck, T. M. (2015). Evolution of a swash zone berm nourishment and influence of berm elevation on the performance of beach-nearshore nourishments along Perdido Key, Florida, USA. *Journal of Coastal Research*, *31*(4), 964–977. https://doi.org/10.2112/JCOASTRES-D-14-00087.1

Camenen, B., & Larson, M. (2006). Phase-lag effects in sheet flow transport. *Coastal Engineering*, *53*(5), 531–542. https://doi.org/10.1016/j.coastaleng.2005.12.003

Craig, R. G. A., Loadman, C., Clement, B., Canada, B. H., Rusello, P. J., & Siegel, E. (2011). Characterization and testing of a new bistatic profiling acoustic Doppler velocimeter: The Vectrino-II. Current, waves and turbulence measurements (CWTM). In *2011 IEEE/OES 10th current, waves and turbulence measurements (CWTM)* (pp. 246–252). IEEE. https://doi.org/10.1109/CWTM.2011.5759559

Dean, R. G., & Dalrymple, R. A. (2002). *Coastal processes with engineering applications*. Cambridge University Press. https://doi.org/10.1017/CBO9780511754500

Dohmen-Janssen, M., & Hanes, D. M. (2005). Sheet flow and suspended sediment due to wave groups in a large wave flume. *Continental Shelf Research*, *25*(3), 333–347. https://doi.org/10.1016/j.csr.2004.10.009

Feagin, R. A., Innocenti, R. A., Bond, H., Wengrove, M., Huff, T. P., Lomonaco, P., et al. (2023). Does vegetation accelerate coastal dune erosion during extreme events? *Science Advances*, *9*(24), eadg7135. https://doi.org/10.1126/sciadv.adg7135

Figlus, J., Kobayashi, N., & Gralher, C. (2012). Onshore Migration of emergent ridge and ponded runnel. *Journal of Waterway, Port, Coastal, and Ocean Engineering*, *138*(5), 331–338. https://doi.org/10.1061/(ASCE)WW.1943-5460.0000139

Goring, D. G., & Nikora, V. I. (2002). Despiking acoustic Doppler velocimeter data. *Journal of Hydraulic Engineering*, *128*(1), 117–126. https://doi.org/10.1061/(ASCE)0733-9429(2002)128:1(117)

Hine, A. C. (1979). Mechanisms of berm development and resulting beach growth along a barrier spit complex. *Sedimentology*, *26*(3), 333–351. https://doi.org/10.1111/j.1365-3091.1979.tb00913.x

Holman, R. A. (1986). Extreme value statistics for wave run-up on a natural beach. *Coastal Engineering*, *9*(6), 527–544. https://doi.org/10.1016/0378-3839(86)90002-5

Horikawa, K., Watanabe, A., & Katori, S. (1982). Sediment transport under sheet flow conditions. In *Presented at the 18th International Conference on Coastal Engineering* (pp. 1335–1352). ASCE. https://doi.org/10.1061/9780872623736.082

Houser, C., & Greenwood, B. (2007). Onshore migration of a swash bar during a storm. *Journal of Coastal Research*, *23*(1), 1–14. https://doi.org/10.2112/03-0135.1

Hughes, M. G., Aagaard, T., Baldock, T. E., & Power, H. E. (2014). Spectral signatures for swash on reflective, intermediate, and dissipative beaches. *Marine Geology*, *355*, 88–97. https://doi.org/10.1016/j.margeo.2014.05.015

IAHR. (1989). IAHR working group on wave generation and analysis: List of sea-state parameters. *Journal of Waterway, Port, Coastal, and Ocean Engineering*, *115*(6), 793–808. https://doi.org/10.1061/(ASCE)0733-950X(1989)115:6(793)

Iribarren, C. R., & Nogales, C. (1949). Protection des ports (Vol. Section II, Comm). In *Presented at the XVII int. Nav. Congress* (Vol. 4, pp. 31–80). PIANC. Retrieved from http://resolver.tudelft.nl/uuid:7ab718ff-a74d-4141-8c3f-413044c751c4

ITTC. (2002). The specialist committee on waves, final report and recommendations to the 23rd ITTC. In *Presented at the 23rd International Towing Tank Conference* (pp. 505–736). Retrieved from https://ittc.info/media/1469/waves.pdf

Jackson, P. D., Smith, D. T., & Stanford, P. N. (1978). Resistivity-porosity-particle shape relationships for marine sands. *Geophysics*, *43*(6), 1250–1268. https://doi.org/10.1190/1.1440891

Jensen, S. G., Aagaard, T., Baldock, T. E., Kroon, A., & Hughes, M. (2009). Berm formation and dynamics on a gently sloping beach; the effect of water level and swash overtopping. *Earth Surface Processes and Landforms*, *34*(11), 1533–1546. https://doi.org/10.1002/esp.1845

Jetté, C. D., & Hanes, D. M. (1997). High-resolution sea-bed imaging: An acoustic multiple transducer array. *Measurement Science and Technology*, *8*(7), 787–792. https://doi.org/10.1088/0957-0233/8/7/014

Katoh, K., & Yanagishima, S. (2015). Berm erosion due to long period waves (pp. 2073–2086). https://doi.org/10.1061/9780872627765.159

Kobayashi, N., Buck, M., Payo, A., & Johnson, B. D. (2009). Berm and dune erosion during a storm. *Journal of Waterway, Port, Coastal, and Ocean Engineering*, *135*(1), 1–10. https://doi.org/10.1061/(ASCE)0733-950X(2009)135:1(1)

Kolmogorov, A. N. (1962). A refinement of previous hypotheses concerning the local structure of turbulence in a viscous incompressible fluid at high Reynolds number. *Journal of Fluid Mechanics*, *13*(1), 82–85. https://doi.org/10.1017/S0022112062000518

Komar, P. D. (1998). *Beach processes and sedimentation* (2nd ed.). Prentice-Hall.

Lanckriet, T. M., Puleo, J. A., Masselink, G., Turner, I. L., Conley, D. C., Blenkinsopp, C., & Russell, P. (2014). Comprehensive field study of swash-zone processes, Part 2: Sheet flow sediment concentrations during quasi-steady backwash. *Journal of Waterway, Port, Coastal, and Ocean Engineering*, *140*(1), 29–42. https://doi.org/10.1061/(ASCE)WW.1943-5460.0000209

Lanckriet, T. M., Puleo, J. A., & Waite, N. (2013). A conductivity concentration profiler for sheet flow sediment transport. *IEEE Journal of Oceanic Engineering*, *38*(1), 55–70. https://doi.org/10.1109/JOE.2012.2222791

Luijendijk, A., Hagenaars, G., Ranasinghe, R., Baart, F., Donchyts, G., & Aarninkhof, S. (2018). The state of the world's beaches. *Scientific Reports*, *8*(1), 6641. https://doi.org/10.1038/s41598-018-24630-6

Masselink, G., & Puleo, J. A. (2006). Swash-zone morphodynamics. *Continental Shelf Research*, *26*(5), 661–680. https://doi.org/10.1016/j.csr.2006.01.015

Mieras, R., Puleo, J. A., Anderson, D., Cox, D. T., & Hsu, T.-J. (2017). Large-scale experimental observations of sheet flow on a sandbar under skewed-asymmetric waves. *Journal of Geophysical Research: Oceans*, *122*(6), 5022–5045. https://doi.org/10.1002/2016JC012438

Mizuguchi, M., & Seki, K. (2015). Field observation of morpho-dynamic processes during storms at a Pacific beach, Japan: Role of long-period waves in storm-induced berm erosion. *Proceedings of the Japan Academy, Series B*, *91*(2), 52–62. https://doi.org/10.2183/pjab.91.52

Mori, N., Suzuki, T., & Kakuno, S. (2007). Noise of acoustic Doppler velocimeter data in bubbly flows. *Journal of Engineering Mechanics*, *133*(1), 122–125. https://doi.org/10.1061/(ASCE)0733-9399(2007)133:1(122)

Myrhaug, D., & Holmedal, L. E. (2007). Mobile layer thickness in sheet flow beneath random waves. *Coastal Engineering*, *54*(8), 577–585. https://doi.org/10.1016/j.coastaleng.2006.11.005

Nielsen, P. (2009). *Coastal and estuarine processes*. World Scientific Publishing Company. https://doi.org/10.1142/7114
Nielsen, P., & Hanslow, D. J. (1991). Wave runup distributions on natural beaches. *Journal of Coastal Research*, *7*(4), 1139–1152. Retrieved from http://www.jstor.org/stable/4297933
NORTEK. (2017). Vectrino profiler. Velocimeter Manual. Retrieved from https://www.nortekgroup.com/export/pdf/Vectrino%20Profiler.pdf
O'Dea, A., Brodie, K. L., & Hartzell, P. (2019). Continuous coastal monitoring with an automated terrestrial lidar scanner. *Journal of Marine Science and Engineering*, *7*(2), 37. https://doi.org/10.3390/jmse7020037
O'Donoghue, T., & Wright, S. (2004). Concentrations in oscillatory sheet flow for well sorted and graded sands. *Coastal Engineering*, *50*(3), 117–138. https://doi.org/10.1016/j.coastaleng.2003.09.004
Osborne, P. D., & Rooker, G. A. (1999). Sand re-suspension events in a high-energy infragravity swash zone. *Journal of Coastal Research*, *15*, 74–86. Retrieved from https://www.jstor.org/stable/4298916
Phillips, M. S., Blenkinsopp, C. E., Splinter, K. D., Harley, M. D., & Turner, I. L. (2019). Modes of berm and beach face recovery following storm reset: Observations using a continuously scanning lidar. *Journal of Geophysical Research: Earth Surface*, *124*(3), 720–736. https://doi.org/10.1029/2018JF004895
Pontiki, M. (2022). *Physics of eroding coastal berm-dune systems during extreme waves and storm surges* (Doctoral dissertation). University of Delaware. Retrieved from https://login.udel.idm.oclc.org/login?url=https://www.proquest.com/dissertations-theses/physics-eroding-coastal-berm-dune-systems-during/docview/2791990057/se-2
Pontiki, M., & Puleo, J. A. (2022). Sediment transport processes across a rapidly eroding bare dune, in physics of dune erosion during extreme surge and wave events [Dataset]. DesignSafe-CI. https://doi.org/10.17603/ds2-csmw-8x65
Puleo, J. A., Faries, J. W. C., Davidson, M., & Hicks, B. (2010). A conductivity sensor for near-bed sediment concentration profiling. *Journal of Oceanic and Atmospheric Technology*, *27*(2), 397–408. https://doi.org/10.1175/2009JTECHO718.1
Puleo, J. A., Krafft, D., Pintado-Patino, J. C., & Bruder, B. (2017). Video-derived near bed and sheet flow sediment particle velocities in dam-break-driven swash. *Coastal Engineering*, *126*, 27–36. https://doi.org/10.1016/j.coastaleng.2017.04.008
Puleo, J. A., Lanckriet, T. M., & Blenkinsopp, C. (2014). Bed level fluctuations in the inner surf and swash zone of a dissipative beach. *Marine Geology*, *349*(1), 99–112. https://doi.org/10.1016/j.margeo.2014.01.006
Russell, P., Masselink, G., Blenkinsopp, C., & Turner, I. (2009). A comparison of berm accretion in the swash zone on sand and gravel beaches. *Journal of Coastal Research*, 1792–1795. Retrieved from http://www.jstor.org/stable/25738098
Shin, C.-H. (2022). Application of the effective diameters of porous media to the non-Darcy flow analyses. *Scientific Reports*, *12*(1), 5321. https://doi.org/10.1038/s41598-022-08135-x
Soulsby, R. L., & Damgaard, J. S. (2005). Bedload sediment transport in coastal waters. *Coastal Engineering*, *52*(8), 673–689. https://doi.org/10.1016/j.coastaleng.2005.04.003
Stockdon, H. F., Holman, R. A., Howd, P. A., & Sallenger, A. H. (2006). Empirical parameterization of setup, swash, and runup. *Coastal Engineering*, *53*(7), 573–588. https://doi.org/10.1016/j.coastaleng.2005.12.005
Suanez, S., Cancouët, R., Floc'h, F., Blaise, E., Ardhuin, F., Filipot, J.-F., et al. (2015). Observations and predictions of wave runup, extreme water levels, and medium-term dune erosion during storm conditions. *Journal of Marine Science and Engineering*, *3*, 674–698. https://doi.org/10.3390/jmse3030674
Sumer, B. M., Kozakiewicz, A., Fredsoe, J., & Deigaard, R. (1996). Velocity and concentration profiles in the sheet-flow layer of the movable bed. *Journal of Hydraulic Engineering*, *122*(10), 549–558. https://doi.org/10.1061/(ASCE)0733-9429(1996)122:10(549)
Suzuki, T., Takeuchi, M., Tomoda, N., Yamaguchi, S., & Kuriyama, Y. (2007). Spatial distribution of cross-shore sediment transport rate for berm formation and erosion. In *Presented at the coastal sediments '07* (Vol. 7, pp. 2037–2048). https://doi.org/10.1061/40926(239)160
Taylor, G. I. (1938). The spectrum of turbulence. *Proceedings of the Royal Society of London. Series A, Mathematical and Physical Sciences*, *164*(919), 476–490. https://doi.org/10.1098/rspa.1938.0032
Turner, I., Russell, P., & Butt, T. (2008). Measurement of wave-by-wave bed levels in the swash zone. *Coastal Engineering*, *55*(12), 1237–1242. https://doi.org/10.1016/j.coastaleng.2008.09.009
van der Zanden, J., Alsina, J. M., Cáceres, I., Buijsrogge, R. H., & Ribberink, J. S. (2015). Bed level motions and sheet flow processes in the swash zone: Observations with a new conductivity-based concentration measuring technique (CCM +). *Coastal Engineering*, *105*, 47–65. https://doi.org/10.1016/j.coastaleng.2015.08.009
Van Rijn, L. C., Tonnon, P. K., Sanchez-Arcilla, A., Caceres, I., & Grune, J. (2011). Scaling laws for beach and dune erosion processes. *Coastal Engineering*, *58*(7), 623–636. https://doi.org/10.1016/j.coastaleng.2011.01.008
Voulgaris, G., & Trowbridge, J. (1998). Evaluation of the acoustic Doppler velocimeter (ADV) for turbulence measurement. *Journal of Oceanic and Atmospheric Technology*, *15*(1), 272–289. https://doi.org/10.1175/1520-0426(1998)015<0272:EOTADV>2.0.CO;2
Wang, P., Brutsche, K. E., LaGrone, J. W., Beck, T. M., Rosati, J., & Lillycrop, L. S. (2013). Performance monitoring of a nearshore berm at Ft. Myers Beach, Florida: Final report. Technical Reports - USACE Digital Library (Final report No. 13–11). Retrieved from https://usace.contentdm.oclc.org/digital/collection/p266001coll1/id/4504/
Wang, Y. H., & Yu, G. H. (2007). Velocity and concentration profiles of particle movement in sheet flows. *Advances in Water Resources*, *30*(5), 1355–1359. https://doi.org/10.1016/j.advwatres.2006.11.012
Wilson, K. C. (1966). Bed-load transport at high shear stress. *Journal of the Hydraulics Division*, *92*(6), 49–59. https://doi.org/10.1061/JYCEAJ.0001562
WW3DG - The WAVEWATCH III® Development Group. (2016). *User manual and system documentation of WAVEWATCH III® version 5.16*. Tech. Note 329, NOAA/NWS/NCEP/MMAB (p. 326). Retrieved from https://polar.ncep.noaa.gov/waves/wavewatch/manual.v5.16.pdf
Yu, Z., Niemeyer, H. D., & Bakker, W. T. (1990). *Site investigation on sand concentration in the sheet flow layer* (pp. 2360–2371). ASCE. https://doi.org/10.1061/9780872627765.180
Zhu, J., Shi, F., Cai, F., Wang, Q., Qi, H., Zhan, C., et al. (2022). Influences of beach berm height on beach response to storms: A numerical study. *Applied Ocean Research*, *121*, 103090. https://doi.org/10.1016/j.apor.2022.103090

Erratum

The originally published version of this article contained a typographical error. In the fourth list item in the Conclusions, "569" should be removed. Item 4 now reads: "Swash zone bed-level changes were more energetic than the bed-level changes in the surf zone. Low-frequency motions had the most impact on mid- to landward-swash bed-level variations." The error has been corrected, and this may be considered the authoritative version of record.